ACS APPLIED MATERIALS & INTERFACES

www.acsami.org

Research Article

Synthesis of Biocompatible Superparamagnetic Iron Oxide Nanoparticles (SPION) under Different Microfluidic Regimes

Jörg Schemberg,* Abdelouahad El Abbassi, Annerose Lindenbauer, Li-Yu Chen, Andreas Grodrian, Xenia Nakos, Gurunath Apte, Nida Khan, Alexander Kraupner, Thi-Huong Nguyen,* and Gunter Gastrock

Cite This: *ACS Appl. Mater. Interfaces* 2022, 14, 48011−48028

Read Online

ACCESS | Metrics & More | Article Recommendations | Supporting Information

ABSTRACT: Superparamagnetic iron oxide nanoparticles (SPION) have a great potential in both diagnostic and therapeutic applications as they provide contrast in magnetic resonance imaging techniques and allow magnetic hyperthermia and drug delivery. Though various types of SPION are commercially available, efforts to improve the quality of SPION are highly in demand. Here, we describe a strategy for optimization of SPION synthesis under microfluidics using the coprecipitation approach. Synthesis parameters such as temperature, pH, iron salt concentration, and coating materials were investigated in continuous and segmented flows. Continuous flow allowed synthesizing particles of a smaller size and higher stability than segmented flow, while both conditions improved the quality of particles compared to batch synthesis. The most stable particles were obtained at a synthesis condition of 6.5 M NH_4OH base, iron salt (Fe^{2+}/Fe^{3+}) concentration ratio of 4.3/8.6, carboxymethyl dextran coating of 20 mg/mL, and temperature of 70 °C. The synthesized SPION exhibited a good efficiency in labeling of human platelets and did not impair cells. Our study under flow conditions provides an optimal protocol for the synthesis of better and biocompatible SPION that contributes to the development of nanoparticles for medical applications.

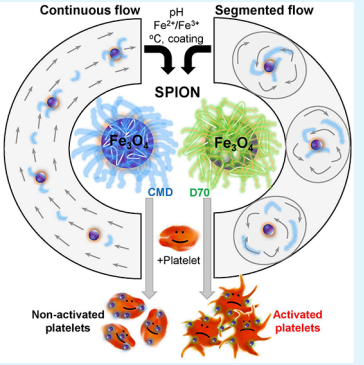

KEYWORDS: *microfluidics, segmented/continuous flow, coprecipitation, SPION, coating, carboxymethyl dextran (CMD), platelet labeling*

INTRODUCTION

For decades, superparamagnetic iron oxide nanoparticles (SPION) have been used in both diagnostic and theragnostic applications such as cell labeling for imaging techniques or drug delivery.[1] In particular, SPION are used in various forms including contrast agents, tissue repair materials, immunoassays, detoxification of biological fluids, hyperthermia, drug delivery, and cell separation.[2] The SPION exhibit multiple advantages such as safe, nontoxic, and biocompatible properties. In diagnostics, SPION have an ability to label various types of cells, including human mesenchymal stem cells, human embryonic kidney 293 cells, or induced pluripotent stem cells,[3] allowing analysis of tissue structures and tracking diseases utilizing magnetic resonance imaging (MRI)[4] or magnetic particle imaging (MPI).[5] The labeled cells can be visualized at a high-resolution level using a fluorescent dye or *via* magnetic properties of the bound particles on cells.[6] Besides, SPION can be used as a heat source in magnetic hyperthermia (MHT), an upcoming new cutting-edge therapy,[7] or as a drug-binding vehicle for cancer treatment.[8] In particular, the combination of SPION with encapsulated polymers that are labeled with the vaccine or a hollow core−shell structure of SPION with gold seeded nanoparticles offers other theranostic approaches.[9,10] As SPION also exhibit antibacterial property, we have successfully integrated them into hydrogel films.[11] The resulting nanocomposite gels inhibited platelet activation, suggesting a promising particle-mixed-material for the development of the platelet storage bag which carries both anti-adhesion and anti-bacterial properties.[11]

Recently, wet chemical processes like sol−gel, pyrolysis, solvothermal, hydrothermal, precipitation, and thermal decomposition have been applied for the synthesis of SPION.[12] The traditional way to produce SPION is the synthesis in batches. This method is limited in terms of reproducibility and specificity because there is less control over parameters during synthesis.[13−15] Microfluidics overcomes these limitations as it enables the synthesis of SPION with narrower size distributions, better reproducibility, and higher drug-loading capacities due to their greater surface-area-to-volume ratios and increased mass and heat transfer.[16,17] Additionally, short diffusion pathways in continuous flow, different forces (shear

Received: July 22, 2022
Accepted: September 28, 2022
Published: October 12, 2022

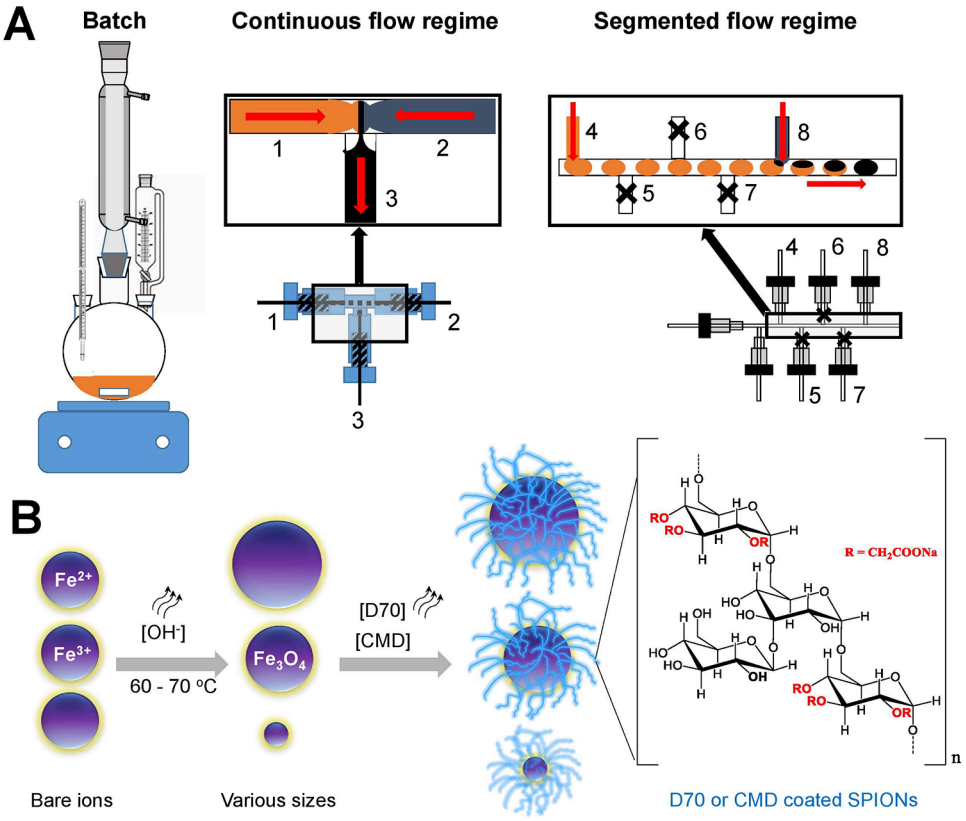

Figure 1. Schematic illustration of the synthesis of SPION under various conditions. (A) Syntheses by (left) batch, (middle) continuous, and (right) segmented flows were investigated. While the process by batch mixes *via* vigorous stirring, the continuous flow mixes by diffusion in a laminar stream, whereas for the segmented flow, a carrier stream with non-immiscible oil transports the generated nL droplet through the main channel. For synthesis under flow, the iron salt (orange: 1 and 4) and base (blue-gray: 2 and 8) were mixed from different channels (black: 3 and 8). The closed side channels 5, 6, and 7 (black cross) are used to increase the distance between the droplets to prevent droplet coalescence. The red arrows indicate the flow direction of the liquid. (B) Cartoons demonstrate synthesis conditions for the development of biocompatible particles coated with dextran 70 (D70) or carboxymethyl dextran (CMD) which have a similar dextran-based structure, except that for D70 R═H, whereas for CMD, R═CH_2COONa.

forces and interfacial tension), and effects (a pinch-off mechanism) in droplet-based regimes with the crossflow as well as flow-focusing setup influence the reaction time and efficiency of the synthesis process.[18−20] Microfluidics is an efficient tool to adjust and control these parameters. The synthesis can be controlled in nanoliter-scale microreactors due to the high level of automation. Typical microfluidic setups are capillary tubing or chips where the channels with a diameter between 100 and 1000 μm are housed in glass, silicon, stainless steel, ceramic, or plastic.[21] These characteristics allow for producing particles with optimized magnetic properties and uniform size/shape. The laminar stream in continuous flow mode allows spatial and temporal control of reactant concentration *via* molecular diffusion, whereas in a segmented flow regime, the rapid mixing is obtained by chaotic advection.[22] In comparison to the traditional synthesis by batch, microfluidics enables a higher production rate with the continuous flow depending on the flow rate.[23] In the meanwhile, the segmented flow setup provides better quality control by employing *in situ* analysis of every droplet within a tube.[24] This facilitates a scale-up of product yield in combination with better control of the production process. To gain maximal efficiency for medical applications, synthetic SPION must meet several criteria, such as superparamagnetic properties and optimal biocompatibility. Even though many efforts have been made to develop SPION under microfluidics,[25] a systematic evaluation with the relevant parameters and more detailed response of SPION to synthetic conditions remains unclear.

Here, we synthesize superparamagnetic iron oxide (Fe_3O_4) nanoparticles under continuous and segmented flow regimes using the coprecipitation procedure. To identify an optimal protocol that allows the synthesis of SPION with high quality, we investigated the effect of different parameters during synthesis on the quality of particles such as temperature, reaction time, pH, iron salt concentration, and polymer coating including carboxymethyl dextran (CMD) and Dextran70 (D70).

The hydrodynamic size distribution and surface ζ potential of the synthesized SPION were characterized using dynamic light scattering (DLS), while iron core diameters were determined by transmission electron microscopy (TEM). The composition of the crystal structure and the crystalline size of the particles were determined using X-ray diffraction (XRD). Thermal stability, polymerization time, thickness of polymer coating, and content of the bound polymer were characterized with thermogravimetric analysis (TGA). The magnetic property was measured using a superconducting quantum interference device (SQUID) magnetometer.

Besides the chemical aspects, we investigated the capacity of particles in the labeling of human blood platelets. Human platelets are developed from the cytoplasm of bone marrow

https://doi.org/10.1021/acsami.2c13156
ACS Appl. Mater. Interfaces 2022, 14, 48011−48028

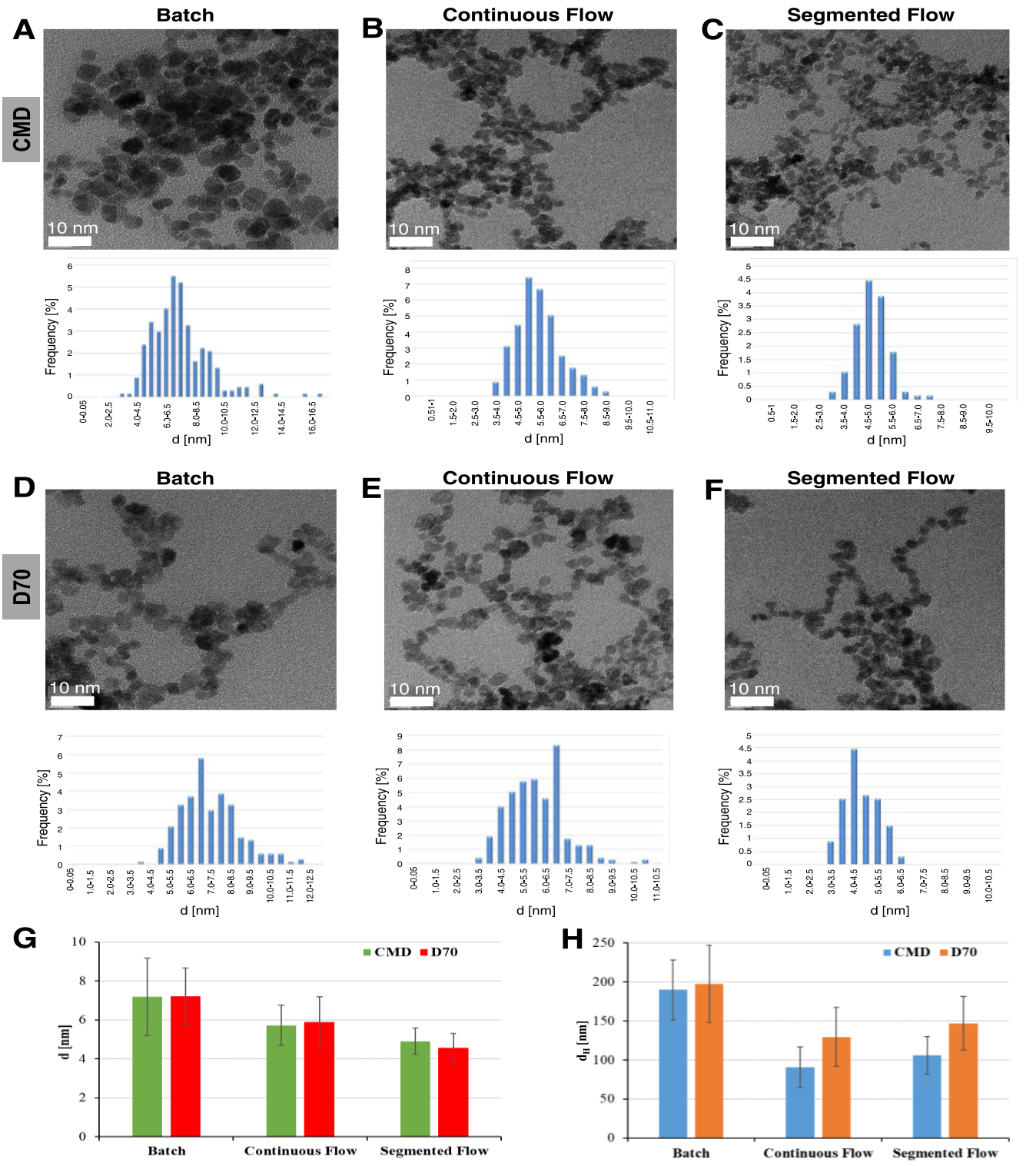

Figure 2. Characteristics of SPION synthesized by batch and under flow. TEM micrographs showed spherical particles synthesized by batch (A, D), under continuous flow (B, E), and segmented flow (C, F) with an iron salt concentration ratio of 4.3/8.65 mM, 6.5 M NH_4OH, and 20 mg/mL CMD (A–C) or D70 (D–F) coating. Histograms below TEM micrographs showed size distributions of corresponding samples. TEM (G) and DLS (H) measurements showed a larger iron oxide core and hydrodynamic diameter (d_H) for particles synthesed by batch as compared with those under flow (I).

megakaryocytes.[26] Platelets are discoid-shaped, anuclear cytoplasmic fragments with a size of 1–2 μm. To prevent or treat bleeding in patients with severe thrombocytopenia or platelet dysfunction, the platelets are transfused. By labeling the transfused platelets with SPION, these cells can be distinguished from the patient's platelets. However, platelets are the most sensitive blood cells that tend to activate immediately after a short contact with artificial[27] and unfavorable surfaces of metals including nanoparticles. This limits many medical applications as activated platelets expose

https://doi.org/10.1021/acsami.2c13156
ACS Appl. Mater. Interfaces 2022, 14, 48011–48028

proteins[28,29] and release prothrombotic substances[30] that together with plasma clotting factors cross-link and activate the surrounding platelets, forming hemostatic plugs at the site of endothelial damage, which eventually results in blood vessel closure. Labeling platelets with radioactive tracers for studies in humans is no longer accepted in many countries.[31] The most promising nonradioactive labeling methodology is the use of magnetic nanoparticles conjugated with proteins such as human serum albumin (HSA).[32] Particle uptake pathway and detailed characterization have been thoroughly understood.[33] Although coating SPION with proteins improved platelet labeling, the process is complex, and HSA coated on particles may result in an excess of albumin in the blood. Fortunately, platelets can endocytose SPION but with lower efficiency.[32,33] This indicates an opportunity for the development of better particles for labeling platelets without involving protein coating. Here, we test the labeling efficiency of platelets with our synthesized SPION to confirm their biocompatible property for medicinal applications *via* the evaluation of morphological changes in platelets using different imaging techniques including confocal laser scanning microscopy (CLMS), white light interferometry (WLI), and scanning electron microscopy (SEM). To determine the content of particles that were uptaken in platelets, atomic absorption spectroscopy (AAS) was utilized. By evaluating the labeled platelets, we were able to identify the synthesis conditions that allow us to generate biocompatible SPION.

RESULTS

Synthesis of Superparamagnetic Nanoparticles under Flow. The magnetic nanoparticles were synthesized under continuous and segmented flows and compared with the ones obtained with the traditional batch synthesis (Figure 1A). In batch (Figure 1A, left), the mixing efficiency of the reactants needs to be enhanced through vigorous stirring. At the beginning of the batch reaction, gradients of different parameters like temperature, pH, or concentration generate due to the nonuniformity of mixing. These changes in local reaction conditions have a strong influence on the nucleation and growth kinetics of the particles and can increase the size distribution of the synthetized particles.[15,34] On the contrary, laminar flow conditions in continuous flow microreactors (Figure 1A, middle), where the mixing efficiency is diffusion-based, induced a spatial and temporal control of reactant parameters.

Due to the chaotic advection inside the droplets or plugs of the segmented flow regime (Figure 1A, right), the diffusion during reaction could not be controlled. The segmented flow microreactors are generated with immiscible liquids, in which the nonpolar medium (oil) as a continuous stream cuts the polar medium, which is the discontinuous stream, by viscous and shear forces. The nonpolar liquid (carrier medium) transports the generated droplets through the main channel. This allows a fast and efficient homogenization of the reaction medium and increases the speed of the reaction.[22] To enhance the biocompatibility of particles, polymers including dextran of 70 kDa (D70) or carboxymethyl dextran of 10 kDa (CMD) which were coated on the surfaces of particles (Figure 1B). This long-chain hydrophilic polymer is composed of glucose with mostly α-1,6 glycoside linkages (Figure 1B).[35] The strong physisorption to magnetic particles occurs in alkaline solution *via* noncovalent interactions of the abundant hydroxyl groups, resulting in enmeshed nanoparticle cores.[36] D70 and CMD have a similar dextran-based structure, except that for D70 R═H, whereas for CMD, R═CH_2COONa (Figure 1B). The hydroxyl groups of D70 can be easily cross-linked and functionalized with primary amines to attach various targeting ligands, peptides, or metal probes. The coprecipitation method employs an alkaline solution such as hard Lewis base (NH_4OH) to precipitate Fe^{2+} and Fe^{3+} ions in an aqueous solution. Magnetite nanoparticles were produced *via* hydrolysis of iron salts to hydroxides as intermediates (reaction 1), followed by dehydration (reaction 2).[37] We applied this well-established coprecipitation method to produce magnetite (Fe_3O_4).

$$2FeCl_3 + FeCl_2 + 8NH_4OH \rightarrow 2Fe(OH)_3 + Fe(OH)_2 + 8NH_4Cl \quad (1)$$

$$Fe(OH)_2 + 2Fe(OH)_3 \rightarrow \mathbf{Fe_3O_4} + 4H_2O \quad (2)$$

To characterize the synthetic magnetic particles, we utilized DLS and TEM as previously described.[13,15,38,39] We first compared the size of particles synthesized by batch and produced under continuous and segmented flows (Figure 2). The synthesis by batch was performed using 4.3 ($FeCl_2$)/8.65 ($FeCl_3$) mM as iron (2+/3+) chloride concentration, 6.5 M NH_4OH at 90 °C, 1 h reaction time under an argon atmosphere, and CMD or D70 as coating as previously described.[40] To avoid liquid evaporation, the temperature and reaction time in the continuous and segmented flow regime (70 °C, 30 min) were lower than synthesis by batch (90 °C, 60 min). TEM micrographs showed that the core size of particles in spherical crystalline shape varied between 4 and 7 nm (Figure 2A−F). The size, size distribution, and shape of particles were comparable with the ones reported previously.[13,41] The Resovist as control showed a hydrodynamic diameter (d_H) of 43.4 nm and a core size of around 5−6 nm. CMD coating resulted in narrower size distribution as compared with D70 coating (Figure 2A−F, lower panels). Averages and standard deviations obtained from different experiments showed that the synthesis by batch produced particles of larger size than the synthesis under flow (Figure 2G−H). The hydrodynamic diameter (d_H), which measured the size distribution of not only the polymer-coated particle but also the hydration shell, showed about 70 nm difference between batch and flow synthesis, whereas a small variance of only a few nm in core diameter was obtained. CMD-coated particles under flow synthesis showed a smallest hydrodynamic size, indicating their highest stability of the dispersion. However, low CMD concentrations (≤5 mg/mL) caused a strong aggregation of particles, while stable particles as indicated by homogeneous samples could be obtained at concentrations ≥10 mg/mL (Figure S1). As particles with small size together with high stability are highly demanded in medical applications, especially, for platelet labeling, we focused in the next experiments only on the synthesis under continuous and segmented flows using 20 mg/mL dextran coating.

To determine the purity of the synthesized particles, we performed an X-ray powder diffraction (XRD) analysis. XRD showed typical patterns for magnetite particles (Figure 3) that confirm the cubic inverse spinel crystal lattice as previously described.[13,15] Consistent with the characteristics of pure Fe_3O_4 from the International Center for Diffraction Data (ICDD file, No. 98-015-8745), our CMD-coated particles

https://doi.org/10.1021/acsami.2c13156
ACS Appl. Mater. Interfaces 2022, 14, 48011−48028

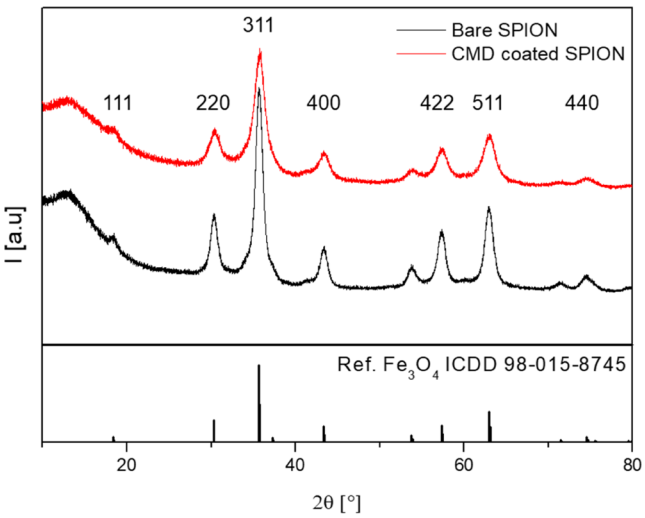

Figure 3. Plotted XRD patterns with signal intensities (I) at different Bragg angles (2θ) for bare (black) and CMD-coated SPIONs (red) together with the diffraction spectrum of pure magnetite from the ICDD database (lower panel).

exhibited magnetite diffraction peaks at (200), (311), (400), (422), (511), and (440) that indicate the high purity of magnetite Fe_3O_4 particles. The magnetite nanoparticle size (D) was calculated *via* the Scherrer formula,[15,42]

$$D = \frac{K\lambda}{B \cos \theta} \tag{3}$$

With the X-ray wavelength (λ = 0.15406 nm), the full width at half-maximum (B) with observed values at 1.036 for bare and 1.760 for CMD-coated SPIONs, the corresponding Bragg angle θ, and the shape parameter (K = 0.89), the crystalline size of the particles was 8.3 nm for bare and 4.8 nm for CMD-coated SPIONs. The obtained sizes are in good agreement with the TEM data (Figure 2) and are comparable with that of Resovist particles described elsewhere.[43]

We next confirmed the successful polymer coating using thermogravimetric analysis (TGA). This technique allows for determining the weight loss of the dried samples according to the melting temperature (T_M). For the CMD-coated SPION, three different steps of weight loss were observed (red, Figure 4A), whereas bare SPION showed only minor weight loss due to physically absorbed water between 70 and 150 °C (black, Figure 4A). In comparison, the first decomposition step was observed at 3−5% weight loss for both particle species due to the loss of physically absorbed water from the particle surface. Two distinct thermal decomposition steps ranging between 250−350 °C and 450−600 °C represent the coated CMD polymer on particle surfaces. The decomposition of the polymer CMD was in total ∼40% with two steps at 10 and 30% weight loss. The higher T_M in comparison to the absorbed water is a typical characteristic of covalent bonds between CMD and particle as described previously.[40,44] The third peak appearing at ∼700 °C indicates the oxidation of magnetite to maghemite (γ-Fe_2O_3). Due to the complete weight loss, the amount of pure magnetite is 55%, meaning that 1 g contains 550 mg of pure magnetite particles.

To determine the magnetization strength of the particles, a superconducting quantum interference device (SQUID) magnetometer was used. Magnetization (M) as a function of magnetic field strength (H) was compared between Resovist and the synthesized particles including bare and CMD-coated SPION (Figure 4B). The mass magnetization curves at the positive field were presented to compare the maximal magnetization values obtained at the saturation parts (10^6−10^7 A/m). The steeper the slope of the curve, the higher the magnetization generated by the particles. Resovist showed a lower level of magnetization than bare SPION but comparable strength as compared with that of CMD-coated SPION. The Resovist is known to have a superparamagnetic property, while our measured magnetization Resovist was consistent with the literature,[40] suggesting that the synthetic particles under flow also exhibit the superparamagnetic property.

We next investigated the effects of different parameters on the quality of synthesized particles under flow, including iron precursor (the iron salt: Fe^{2+}/Fe^{3+}), pH (base concentration), temperature, reaction time, and coating material.

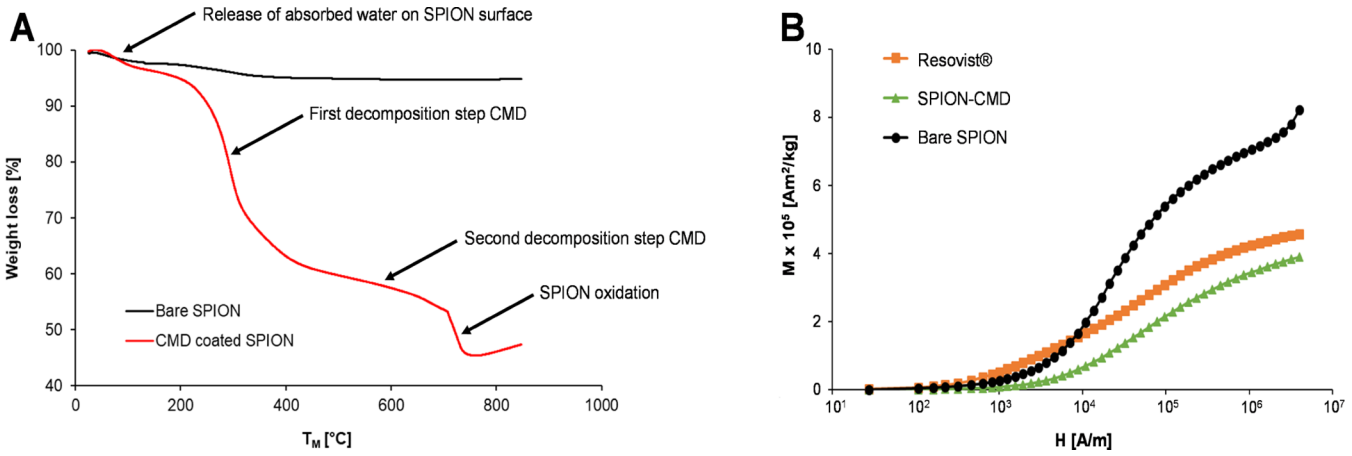

Figure 4. Confirmation of CMD-coated particles and determination of magnetic strength of SPION synthesized under continuous flow. (A) Weight loss curve [%] obtained for bare SPION (black) and CMD-coated SPION (red) by TGA at a temperature of up to 800 °C. Several steps of weight loss were seen ranging from the release of absorbed water and the first/second CMD decompositions to the oxidation of magnetite to maghemite. The first and second decomposition steps indicate that CMD was splitted from the particle surfaces. (B) Magnetization (M) trend as a function of magnetic field strength (H) measured using a SQUID magnetometer showed highest M-value for bare SPION (black), followed by Resovist (orange), and lowest for CMD-coated SPION (green). Note: magnetization curves were not normalized to magnetic material.

https://doi.org/10.1021/acsami.2c13156
ACS Appl. Mater. Interfaces 2022, 14, 48011−48028

Effect of Iron Salt (Fe^{2+}/Fe^{3+}) Concentration. As iron concentration, pH, and the ratio of ferrous and ferric ions directly affect the generation of magnetite (Fe_3O_4) or maghemite (γ-Fe_2O_3) in synthesis by batch,[13] we investigated their effect on the quality of particles synthesized under both continuous and segmented flow conditions. The most suitable conditions including pH 10.2 (6.5 M NH_4OH), 20 mg/mL CMD coating, and a temperature of 70 °C were first selected. Synthesized particles at three different iron salt concentrations including 4.3/8.6, 6.0/12.0, and 8.6/17.3 mM ratios were then compared. It is known that synthesis at an iron salt ratio <0.5 (i.e., 4.3/8.6 mM) results in different intermediate iron oxide products such as FeO or Fe_2O_3 that cause magnetite impurities (goethite), while at iron salt ratio >0.5, the product quality reduces.[45]

Thus, too low and too high iron salt ratios were not investigated in this study. We found that the size of particles increased with increasing iron salt concentration, while their negative surface ζ potential reduced under both continuous and segmented flows (Figure 5). However, continuous flow

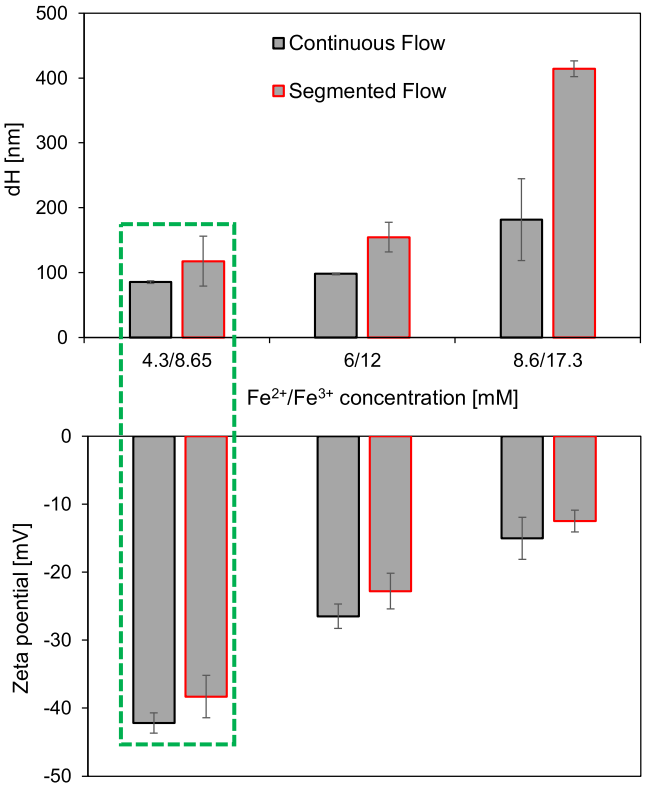

Figure 5. Effect of iron salt ratio on the synthesis of SPION characterized by DLS. Under continuous (black) and segmented (red) flows, the iron salt concentration caused changes in the size (top) and surface ζ potential (bottom) of SPION (reaction time: 30 min, temperature: 70 °C, and base concentration: 6.5 M NH_4OH). The iron salt ratio of 4.3/8.6 mM provided particles of the smallest size and highest negative ζ potential (green).

allows us to synthesize particles with smaller hydrodynamic size and higher negative ζ potential than the segmented flow (Figure 5). The best particles were obtained at the iron salt ratio of 4.3/8.6 mM at which the size d_H was around 100 nm and the ζ potential was approximately −42 mV.

Effect of Base Concentration. Next, the iron salt ratio of 4.3/8.6 mM was kept constant, while other parameters such as temperature, base (NH_4OH) concentration, and polymer coating were varied. We synthesized SPION under three base concentrations of 3.9, 6.5, and 12.9 M NH_4OH, which correspond to pH 9.5, 10.2, and 10.8. At this pH range, the size of the colloidal suspension of magnetite is smaller than that in the lower pH range, which guarantees a regular nucleation and growth process for the desired magnetite (Fe_3O_4).[13]

The hydrodynamic size and surface ζ potential of the particles determined by DLS at the particle concentration of 0.8 mM showed that the base concentration governed the size of the SPION (Figure 6). The largest sizes were found when the SPION were synthesized at either low (3.9 M NH_4OH) or high (12.9 M NH_4OH) base concentration, and much smaller sizes were obtained at the intermediate base concentration (6.5 M NH_4OH) (Figure 6A). The segmented flow induced larger particles than the continuous flow at ≥6.5 M NH_4OH, whereas no significant difference was found at 3.9 M NH_4OH. All SPION showed a high negative surface ζ potential ranging between −48 and −65 mV (Figure 6B). Overall, the continuous flow allowed the synthesis of particles of the smallest size and high negative surface ζ potential that can enhance the stability of the SPION.

Effect of Reaction Time and Temperature on Synthesized Particles. Based on previous studies showing that the complete growth process for magnetite nanoparticles is fast (~8 min) and the digestion time is until 60 min,[13] we screened the reaction time between 30 and 60 min. With the appropriate synthesis conditions (pH, iron salt concentration, temperature), we did not observe significant differences in particle size within this reaction time (data not shown). At temperatures higher than 80 °C, evaporation effects of the base (NH_4OH) during the reaction process occur that alter the 1/2 stoichiometric relation of (Fe^{2+}/Fe^{3+}), which can result in a strong agglomeration of the generated SPION. At temperatures lower than 60 °C, pH needs to be increased to 10.8 to maintain the iron salt concentration ratio.[15] Higher temperatures cause decreases in oxygen solubility in an aqueous solution. This favors the degree of crystallinity for generating magnetite.[14] Therefore, we focused on the most suitable temperature range between 60 and 70 °C under continuous flow at intermediate pH (6.5 M NH_4OH). SPION synthesized at 60 °C exhibited a larger size (Figure 7A) and slightly higher negative surface ζ potential (Figure 7B) than those produced at 70 °C. The results indicated that better quality of particles could be produced at 70 °C, and therefore, this temperature was chosen for the next experiments.

The stability particles stored at 6 °C were tracked over time within 19 months using DLS. High stability for polymer-coated SPION in both batch and microfluidics was observed (Figure S2). The only difference among microfluidic regimes was the slightly higher hydrodynamic diameter for segmented flow conditions.

Effect of Polymer Type and Their Concentration. For the enhancement of the biocompatibility and stability of the SPION, we compared the hydrodynamic size and stability of the dispersion of particles *via* surface ζ potential when particles were coated with 5, 10, and 20 mg/mL CMD or D70. A strong aggregation in the sample when particles were coated with ≤5 mg/mL was observed (Figure S1), and therefore, dextran of lower than this concentration was excluded from further investigation.

Comparison of Characteristics of Synthesized Particles under Various Conditions. To identify the stability of the

https://doi.org/10.1021/acsami.2c13156
ACS Appl. Mater. Interfaces 2022, 14, 48011−48028

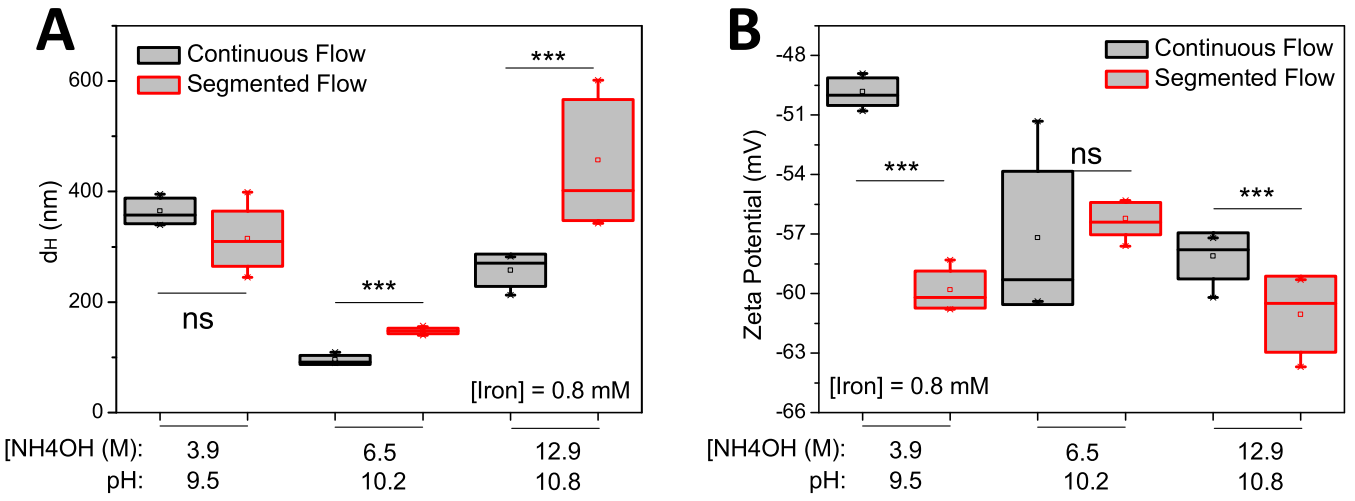

Figure 6. Synthesis of CMD coated SPION under various pH conditions. (A) At 0.8 mM iron concentration, the size of the particles increased as pH developed, whereas (B) surface ζ potential showed a reverse trend. Statistics were performed with one-way analysis of variance (ANOVA) test, ***significant difference ($P < 0.05$), ns = no significant difference ($P > 0.05$) ($n = 5$ repetitions).

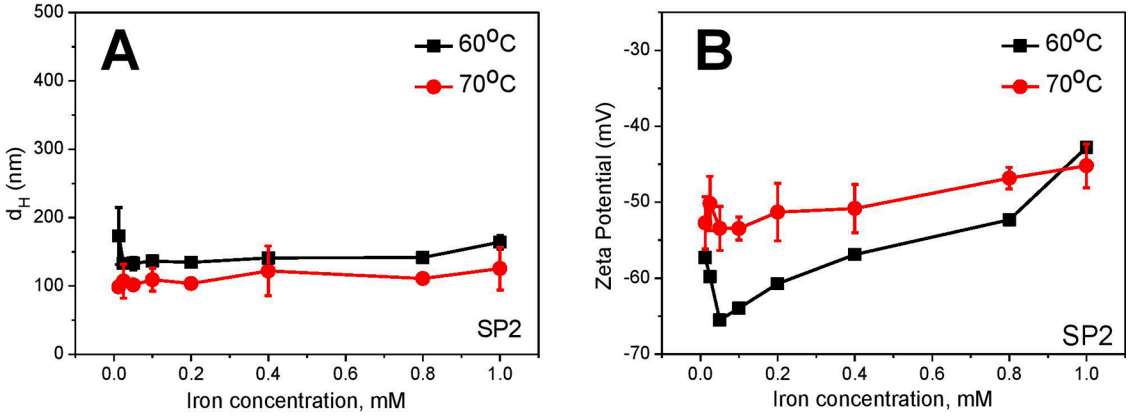

Figure 7. Effect of temperature on synthesized SPION coated with CMD. (A) The synthesized particles at 60 °C (black) exhibited a larger size and (B) higher negative surface ζ potential than those at 70 °C (red) at the base concentration of 6.5 M NH_4OH.

dispersion of particles, we titrated SPION of different concentrations up to 1.0 mM into water and compared their size and surface ζ potential (Figure 8). All particles synthesized at various base concentrations (3.9, 6.5, and 12.9 M) and coated with either CMD or D70 under continuous and segmented flow were plotted for comparison. Both investigated parameters varied depending on the synthesized condition.

Within the range of 1 mM iron concentration, the size of particles did not significantly change for all conditions under continuous flow (Figure 8A), but a strong variation was observed at iron concentrations $\leq$0.35 for particles synthesized at low base (3.9 M NH_4OH) or $\leq$0.16 mM for ones produced at the high base with CMD coating (12.9 M NH_4OH) (blue, Figure 8B). The results indicated lower stability of the dispersion of particles at these low and high pH conditions. Interestingly, the size of D70-coated SPION was comparable with CMD-coated particles at different base concentrations in both flow regimes (Figure 8A,B). The CMD-coated SPION showed higher negative surface ζ potential (*i.e.*, between −40 and −70 mV) than that of D70 (*i.e.*, ranging between +10 and −20 mV). Most probably, D70 coating induced aggregation of particles. High negative ζ potential indicates a higher repulsive effect that leads to more stability of the dispersion among particles. The CMD coating particles showed higher stability of the dispersion than the D70 (Figure 8C,D). Continuous flow did not but the segmented flow clearly showed an exponential dependence of ζ potential as a function of iron concentration (Figure 8C,D). Except D70 coating at high pH, synthetic particles exhibited ζ potential values around −40 mV, indicating the high stability of the particle dispersion. At pH 10.8 (12.9 M NH_4OH), the segmented flow also caused a strong effect on the stability of the dispersion of the SPION. The particles synthesized at high base concentrations were less stable than the ones produced at the lower base condition, especially for D70 coating (Figure 8D).

Overall, the condition to produce the most stable SPION was determined at (i) 6.5 M NH_4OH, (ii) CMD coating with a concentration of 20 mg/mL, (iii) 70 °C, (iv) an iron salt concentration ratio with 4.3 mM (Fe^{2+})/8.6 mM (Fe^{3+}), and (vi) under both continuous and segmented flow conditions. However, the continuous flow allowed the synthesis of SPION of a smaller size than the segmented flow. To simplify, we named SPION (SP) samples as SP1, SP2, SP3, and SP4 for those synthesized under continuous flow at different conditions (Table 1).

Ability of Synthesized SPION in Labeling Platelets. Many efforts for labeling platelets with SPION have been recently made to distinguish between transfused platelets and

https://doi.org/10.1021/acsami.2c13156
ACS Appl. Mater. Interfaces 2022, 14, 48011−48028

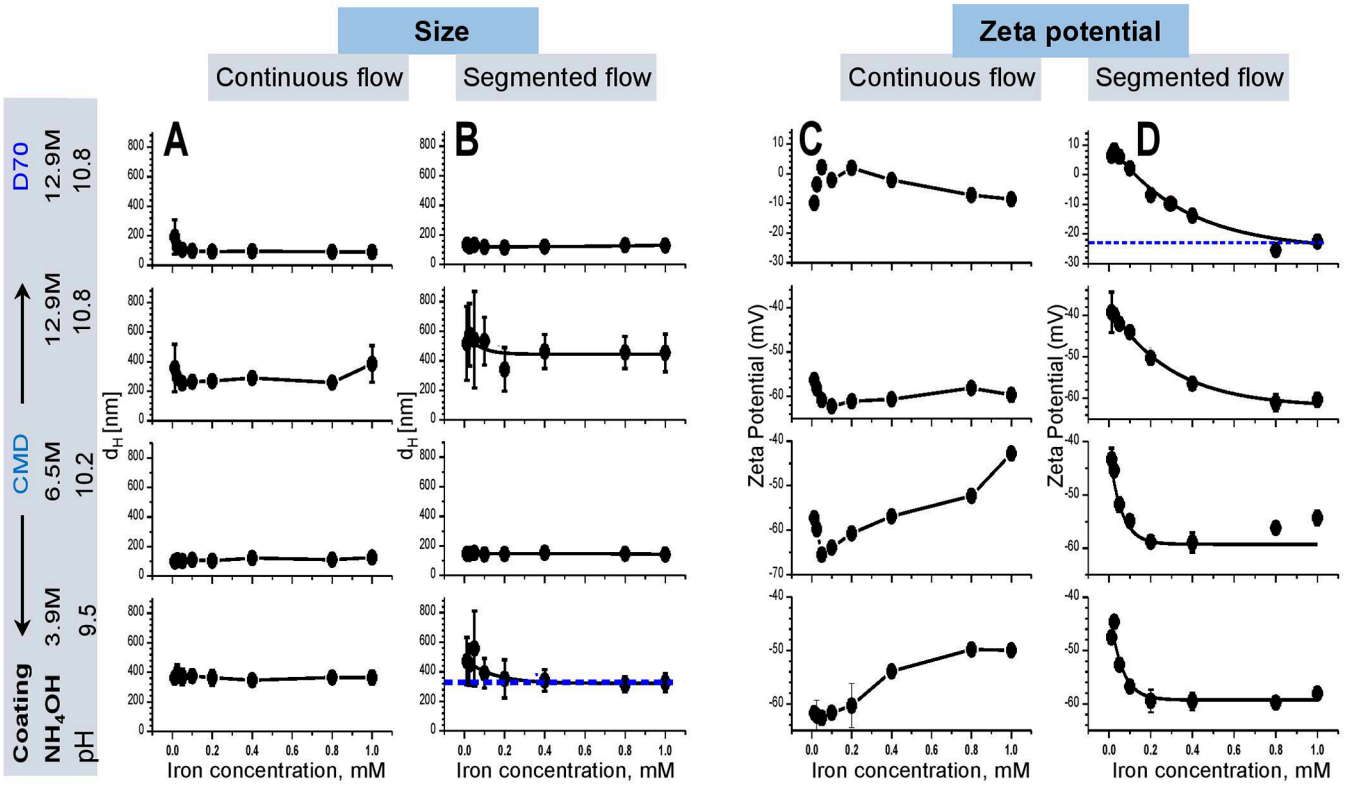

Figure 8. Comparison of the stability of SPION dispersion among particles synthesized at different conditions. (A) Continuous flow provided a smaller SPION size than (B) segmented flow, especially at low (3.9 M) and high (12.9 M) NH_4OH concentrations (guided by blue line). (C) Continuous flow did not show an exponential decay of surface ζ potential, whereas (D) segmented flow did, indicating is lower than −40 mV (guided by blue line).

Table 1. Overview of the Best Conditions for SPION Synthesis under Continuous Flow

SPION (SP)/characteristics			base condition		polymer (mg/mL)		
Name	d_H (nm)	ζ potential (mV)	NH_4OH [M]	pH	CMD	D70	Fe^{2+}/Fe^{3+} (mM)
SP1	135.5 ± 32.9	−(40 to 62)	3.9	9.5	20		4.3/8.6 (molar ratio = 0.5)
SP2	90.5 ± 26.2	−(40 to 62)	6.5	10.2	20		4.3/8.6 (molar ratio = 0.5)
SP3	155.1 ± 35.2	−(40 to 62)	12.9	10.8	20		4.3/8.6 (molar ratio = 0.5)
SP4	152.7 ± 126.6	−21 to +10	12.9	10.8		20	4.3/8.6 (molar ratio = 0.5)

patient's own platelets.[32,46] Therefore, testing ability of the newly developed SPION in labeling platelets to identify particles that do not impair cell's function is highly demanded. We selected this most sensitive cell type to identify the reactivity of our synthesized particles as a hint for future *in vivo* studies (Table 1).

We labeled platelets with particles and stained them with anti-CD42a conjugated antibody for visualization by confocal laser scanning microscopy (CLSM) (Figure 9). The resulting images showed different morphologies of platelets (red dots) depending on the characteristics of added agents (Figure 9). The nonlabeled platelets showed round shapes and are separated from each other (Figure 9A), which were comparable to the shape of platelets labeled with carboxy dextran particles (Resovist) (Figure 9B). When the platelets were activated by thrombin receptor-activating peptide (TRAP) as a positive control, they changed their shapes and formed aggregation (Figure 9C). The platelets manifest themselves as small round shapes (Figure 9A, red dots), but they changed their shape which can be visualized as a fluorescent shadow around the platelets. Interestingly, CMD-coated particles (SP1−3) induced minimal changes in platelet morphologies (Figure 9D−F), whereas D70 (SP4) caused platelet activation and aggregation (Figure 9G). The distinct effect might result from the surface property of the particles. The SP4 with D70 coating exhibited a ζ potential close to zero, whereas CMD-coated particles (SP1−3) exhibited a ζ potential of approximately −40 mV. The suspension of SP4 was not sufficiently stable, resulting in an agglomeration that led to platelet aggregation. Quantification of the size of single platelets also showed the weakest change by SP2, followed by SP3, and the strongest increase by SP1 (Figure 9H). The size of single platelets in the presence of SP4 and TRAP was not possible to quantify due to platelet aggregation. Thus, we dried the samples and imaged them with scanning electron microscopy (SEM) (Figure S3) and white light interferometry (WLI) (Figure S4). The images showed changes in platelet morphology in SEM and roughness (Sa) of labeled platelets in WLI. Quantification of the roughness shows a similar value among platelets alone, and SP3, higher for SP1 and SP4 but highest for TRAP. This indicates that aggregation of platelets was triggered by TRAP and some effects caused by SP1 as well as SP4, but SP2 did not cause any damage. As fluorescent labeled CD62P on the platelet membranes, while nanoparticles

https://doi.org/10.1021/acsami.2c13156
ACS Appl. Mater. Interfaces 2022, 14, 48011−48028

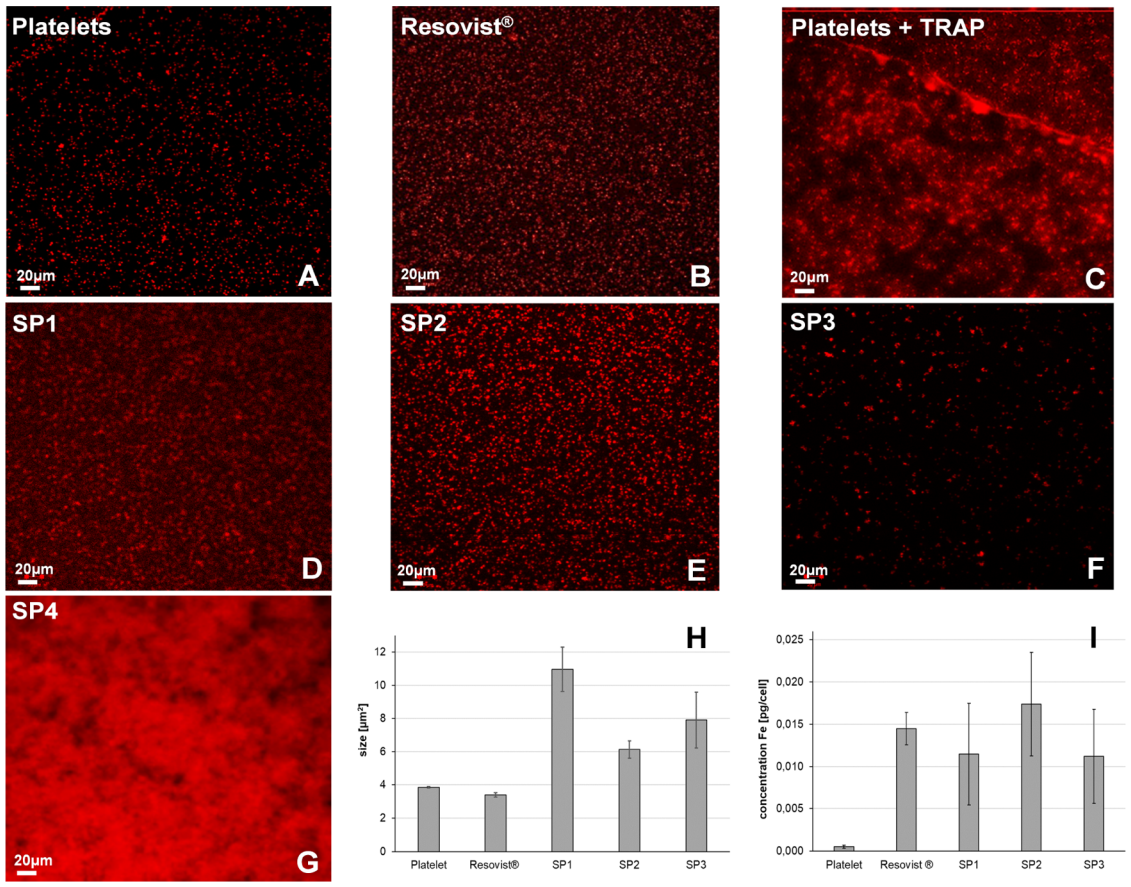

Figure 9. Characteristics of platelets labeled with different types of SPION by CLSM and AAS. Platelets (red) stained with anti-CD42 antibody fluorescent for CLSM imaging showed no aggregation in the (A) absence of particles, whereas (B) Resovist showed strong aggregation/activation induced by (C) TRAP, a positive control, and (D−G) variation of platelet sizes induced by SPION. (H) Quantification of the size of platelets after labeling with SPION showed the largest size of platelets caused by SP1, followed by SP2 and SP3, and the smallest size by Resovist and platelet alone. Strong activation of platelets by TRAP and SP4 did not allow quantification of platelet sizes, and they linked to each other. (I) The iron concentration, which was uptaken inside the platelets determined by AAS showed the highest value for SP2, followed by Resovist, lower for SP1 and SP3, and lowest for platelets without particles added.

were located inside the platelets, we attributed that the possibility of fluorescence quenching by particles during the investigation was minimal.

To identify the efficiency of the synthesized SPIONs in labeling platelets, platelets were incubated with particles at 37 °C. After removing unbound particles in the suspension, iron content per labeled platelet was determined by atomic absorption spectroscopy (AAS). The most effective labeling was obtained with SP2, followed by Resovist, SP1, and lowest for SP3, while the platelet alone as a control showed minimal iron concentration as background (Figure 9I). The results again confirmed that the synthesis condition for SP2 provides the best quality.

DISCUSSION

We have successfully optimized a protocol for the synthesis of SPION under flow conditions. Synthesis under flow provided a better quality of particles than by batch. The continuous flow improved the quality of SPION compared to the segmented flow. An optimal condition for the synthesis was identified at 70 °C, pH 10.2 (=6.5 M NH_4OH), iron salt ($FeCl_2/FeCl_3$) concentration of 4.3/8.6 mM, and coating carboxymethyl dextran (CMD) of 20 mg/mL. At this optimized condition, particles of small size, excellent stability, and biocompatibility could be produced.

The advantage of efficient mixing of the reactants was obtained by small diffusion path length in continuous flow within nL droplets by the segmented flow.[22] This allowed synthesizing SPION of accurate sizes and high quality that could be proved by multiple methodologies such as TEM, DLS, XRD, and TGA. Consistent with the previous synthesis by batch,[13] pH together with the ionic strength of the reactants had the greatest influence on the size and size distribution, followed by the iron precursor concentration, with a Fe^{2+}/Fe^{3+} molar ratio of 0.5. Furthermore, the operating temperature varied the particle size, whereas the amount of polymer-coating agent governed the stability of the particles during the synthesis process, which is consistent with the previous report on synthesis by batch.[47]

A previous study reported that screening of the reaction time between 30 and 60 min showed negligible effects.[13] Within the sealed microfluidic setup, we could reduce the reaction time and temperature applied in batch synthesis from 60 min and 90 °C to 30 min and 70 °C. The shorter reaction time and lower temperature avoid evaporation and bubbling effects generated from the educt NH_4OH. The bubbling can disturb the droplet generation during the synthesis process in the segmented flow regime. The conventional reaction by batch requires inert gas (N_2, Ar) to prevent uncontrolled oxidation processes that cause a change in the initial molar ratio of the

https://doi.org/10.1021/acsami.2c13156
ACS Appl. Mater. Interfaces 2022, 14, 48011−48028

iron precursors.[48] Microfluidic setup with its small reaction volume from μL till nL scale reduces the operating temperature during the synthesis. Due to sealed chips and tube modules, the continuous and segmented flows do not need inert gas to prevent oxidation effects. Importantly, CMD-coated particles synthesized under flow showed long time stability of up to 19 months (Figure S2).

pH showed a significant effect on the size of particles synthesized under both continuous and segmented flows. For high (12.9 M NH_4OH) and standard (6.5 M NH_4OH) base concentration, the continuous flow allowed to produce smaller particles than the segmented flow, while at the low base concentration (3.9 M NH_4OH), a reversed trend occurred. This can be interpreted with the differences in the mixing mechanism of the reactants, nucleation, and growth kinetics of particles. Based on the theory of colloidal formation by La Mer et al.,[49] the uniform particle generation needs an appropriate reaction time until the saturation of the produced particles is reached. To avoid precipitation, the reaction needs to be fast enough, so that the saturation limit exceeds before the precipitation begins.[50] In this supersaturation phase, initial particles act as seeds or nucleation cores for the final products. Additional particles developed on the surface of particles until reaching the final SPION. The size and their distribution depend on the number of particles developed on the nucleation seeds. The more particle seeds are produced, the smaller the particle size will be.[51] Additionally, the charge distribution in the medium is essential for the kinetics of the nucleation and growth process. Due to the diffusion-based mixing, in the continuous flow, the reaction time is reduced in comparison to the segmented flow regime where the mixing is chaotic. For the higher base concentration than 3.9 M NH_4OH, the enhanced ionic strength by the OH^- ions reduced the saturation limit. Initial seeds can be produced faster and a higher amount before the growth process begins. For segmented flow, the particle growth begins before the nucleation process is complete. The more or less uncontrolled process needs to be limited with more exact dosing of the relevant reactants. In contradiction to batch,[13] the size differences in microfluidics caused by temperature can be described with the higher amount of particle seeds that can be built at a higher temperature.

The dependency of the coating concentration for the particle size indicates that the bigger the coated particle, the fewer precipitation effects occur. These results follow the theory of steric stabilization that builds barriers between the particles.[50] The long chain of the coated molecules has a high affinity for the solvent. This makes it energetically unfavorable that solvent will be eliminated among particles and from the surrounding chains. Especially, the difference between CMD and D70-coated SPION in size and size distribution can be described with the higher negative charge (hydroxyl and carboxyl groups)[44] and the lower molecular weight of CMD (10 kDa) than D70 (70 kDa). Therefore, stronger electrostatic repulsion effects due to the higher negative charge of CMD between the adjacent coated SPION can be a reason.

The ζ potential trend for the continuous flow regime shows a minimal variation of the negative charge with increasing particle concentration until a stable plateau at around −50 mV. At a low SPION concentration, a higher amount of small nanoparticle seeds together with CMD and D70 generated the total amount of charge. In this condition, a higher ratio of negatively charged ligands like hydroxyl (OH^-) and carboxyl (COO^-) groups dominated in the aqueous solution. With higher SPION concentration, the nanoparticle seed concentration decreased, while the growth process of the nanoparticles occurred and covalent binding events between the carboxyl groups of CMD and -OH groups of D70 and the iron precursor led to a constant charge quantity. The reason for such an effect could be different in the charges between unbound and particle-bound ligands. On the contrary, with the segmented flow, the negative charge from particle-bounded carboxyl groups of CMD increases with the increase of SPION concentration until a constant value of −60 mV. The lesser amount of charge at the lower SPION concentration is the dilution effect of water. With the same parameters (iron concentration, pH, and temperature), the continuous flow regime has fewer bounded CMD particles (−50 mV) than the segmented flow. This implies that the binding and mixing efficiency in these regimes differ. In summary, we found that the ζ potential differed depending on the mixing mechanism at each fluidic regime, *i.e.*, faster mixing *via* the segmented flow (chaotic mixing) in comparison with the continuous flow (diffusion based on laminar flow) has some effect on the binding mechanism of the CMD ligands to the SPION surface. This effect has been confirmed in several studies of nanoparticle synthesis in flow.[52]

In continuous flow, mixing occurs through diffusion. Due to the parabolic flow profile in the microchannels, nonhomogeneous diffusion over the channel height and low mixing efficiency can occur. To create a good mixing design, chaotic mixers or 3-D chips that can be split and put back together (split and recombine design) are necessary.[53] In segmented flow, enhanced mixing *via* chaotic advection is obtained in droplets. The mixing efficiency depends on parameters like capillary numbers, the ratio of viscosities of the dispersed and the continuous phase, the ratio of the drop diameter and the channel width, and the meandering shape of the channel design.[54] After the generation of droplets with the iron salt solution, the reaction starts immediately after the dosing with the base inside the iron salt droplets. This fast and efficient homogenization enhanced the reaction time in contrast to the design in continuous flow. This explains the slightly smaller size of the SPION obtained in continuous flow in comparison to those in segmented flow which is an advantage in the direction of minimization of particle size. The disadvantages of such a homogenous synthesis that influences the size distribution are the clogging effects of the channels, which need to be overcome with a special glass capillary injection design or reaction with ultrasound.[55,56] The clogging problems inside the channels have a strong impact on the magnetic properties of the resulting nanoparticles. However, the mechanism of the aggregation effect for iron oxide nanoparticles has not yet been well understood and needs to be further investigated.

By measuring the hydrodynamic diameter (d_H) by DLS, the aggregation could be identified if two size distributions appear. Besides colloid forming forces (electrostatic, van der Waals), dipole−dipole or exchange interactions play a key role by generating agglomeration processes as interparticle distance decreases and dipolar interactions increase, while a collective magnetic state is formed.[57] Synthetized SPION exists in the form of colloids, also termed as dispersions or solid−liquid systems. Without surface coatings and in the absence of an external field, SPION tend to gather forming groups of several magnetic cores generally called aggregates. In an irreversible

https://doi.org/10.1021/acsami.2c13156
ACS Appl. Mater. Interfaces 2022, 14, 48011−48028

process, magnetic cores will remain together, whereas formation of alterable agglomerates may occur in the reversible process. Several processes lead to a mixture of isolated SPION and their appropriate nanoclusters.[58] The water phase stabilization is a necessary process to avoid nanoparticle clustering in the aqueous phase. The colloid stability is governed by a balance between attractive (dipolar and van der Waals) and repulsive electrostatic and steric interactions and is influenced by pH, ionic strength, or medium composition (*e.g.*, salt concentration).[59] As a result of aggregation processes, interparticle distances decrease and dipole−dipole interactions (long distance interactions), whose strength depends on the distances, increase.[60] Depending on the orientation of the particles forming the aggregate/agglomerate, either random orientation or with alignment of the magnetic moments (*e.g.*, forming chains), these interactions may be significantly different.[61] Increasing dipole−dipole interactions during the agglomeration mechanism have a significant influence on magnetization measurements, resulting in a change of hysteresis loop,[62] a shift of the zero-field-cooled maximum toward a higher temperature,[63] and a similar displacement of the blocking temperature appears on alternating current measurements of interacting nanoparticles.[64] Exchange interactions are especially relevant in the case of multicore particles prepared directly with a controlled aggregation of the cores, forming nanoflowers.[65] The exchange interactions (short-range interactions) involve the coupling of the magnetic moments from two neighbor atoms. In nanoflowers, there is a crystal continuity at the core interfaces that allows a cooperative behavior due to exchange interactions between the cores, resulting in an enhanced susceptibility while maintaining superparamagnetic behavior.[65]

Only a slight difference in the curve progression by a SQUID magnetometer indicated that our synthetic particles by flow provided an approximately equal level of superparamagnetic strength as compared with Resovist. However, bare SPION exhibited higher magnetization efficiency than CMD-coated SPION and Resovist. The reason is the shielding effect of the polymers during the magnetization process.[66] Analysis by TEM and DLS underlines the better SPION quality in size and size distribution by the microfluidic synthesis in comparison to batch. The XRD patterns showed a high purity of the synthesized SPION with the crystalline size of 8.3 nm (bare SPION) and 4.8 nm (CMD-coated SPION) in accordance with the TEM data indicating that the synthesis process for the generation of pure magnetite in the microfluidic platforms was successful. In particular, the coprecipitation synthesis method *via* Massart under continuous flow showed better particle performance than in segmented flow. The reason can be the passive dosing of the base into the droplet of segmented flow where the reaction occurs immediately. Due to the very small pressure differences in the microchannels, the number of dosed reactants can vary. Hence, an automatized active dosing should increase the precision of the mixed reactants, which leads to a better quality of the resulting particles. The TGA results confirmed the characteristic thermal decomposition curve for CMD-coated SPION in comparison to bare particles described elsewhere.[44] The curve showed several steps of weight loss including the evaporation of physically adsorbed water at 70−150 °C, the polymer decompositions at 250−350 °C and 450−600 °C, and the oxidation of magnetite at ∼700 °C.[40] As CMD has been firmly coated to nanoparticle surfaces, high energy is required to break down the covalent bonds before degradation of the coating (first and second decompositions, Figure 4).[67] After CMD decomposes completely, the residue that remains is composed mostly of bare SPION. An estimation of the polymer content (CMD) was done. The weight loss (%) for CMD-coated SPION was estimated to be in total approximately 40%, whereas for bare SPION only 3−5% due to the loss of physically absorbed water. The complete weight loss of ∼45% means that SPIONs have an amount of ∼55% pure magnetite. Another interesting behavior of CMD coated with SPION was observed with increasing CMD concentration that their chains become more tangled on the surface of SPION.

Besides the chemical aspects, we investigated the biological applicability of the synthesized particles in the labeling of human blood platelets. Platelet labeling with a nonradioactive tracer is highly demanded to distinguish between transfused and patients' own platelets according to ethical issues in many countries.[31] Coating magnetic nanoparticles with albumin enhanced platelet labeling efficiency.[32,33] However, the complex protein coating process and the release of albumin in blood circulation can be a drawback. Thus, improvement of the quality of particles for platelet labeling without involving proteins becomes another interesting aspect. Our synthesized SPION showed different capacities for labeling platelets depending on particle characteristics. With a size of around 100 nm (the SP2), particles penetrate or absorb efficiently into the platelets. The particles coated with CMD did not induce platelet aggregation, whereas the ones coated with D70 strongly induced aggregation of platelets. The surface ζ potential (around −60 mV) of CMD-coated SPION caused strong particle repulsion, whereas the surface ζ potential (zero) of D70-coated particles caused SPION aggregation. As platelets are extremely sensitive and can be activated immediately when contacting nonphysiological surfaces,[27,68,69] the resulting large aggregated D70 particles together with their zero surface ζ potential likely facilitated platelet aggregation and activation.

The synthesized particles coated with CMD (20 mg/mL) at different pH affected the platelets differently, depending on their size and surface charge. Particle sizes were around 400, 100, and 230 nm at low (pH 9.5 or 3.9 M NH_4OH), medium (pH 10.2 or 6.5 M NH4OH), and high (pH 10.8 or 12.9 M NH4OH) base concentrations, respectively. The particles of the largest size (∼400 nm) caused the strongest activation of platelets, followed by the medium size (∼230 nm), and the weakest by the ones with the smallest size (∼100 nm). The yield of platelet labeling as determined by iron concentration per platelet was highest by particles of the smallest size (SP2 ∼100 nm) (Figure 8I). These results indicate that the size of particles plays an important role in platelet labeling. With Resovist and albumin-coated particles, we have previously described[33] that the particles diffuse into open canalicular system (OCS) channels of platelets as observed by TEM imaging. By measuring binding forces between single particle and platelets, we observed both strong and weak binding forces that allowed us to conclude that the particle could travel inside platelets, but some of them are also bound on the platelet membranes. Due to the small size of platelet OCS, only small particles can enter the OCS gates, while particles with a larger size than the width of the OCS will not be able to diffuse into platelets. This explains our results that the highest iron concentration was obtained by labeling platelets with SP2 of d_H ∼100 nm.

https://doi.org/10.1021/acsami.2c13156
ACS Appl. Mater. Interfaces 2022, 14, 48011−48028

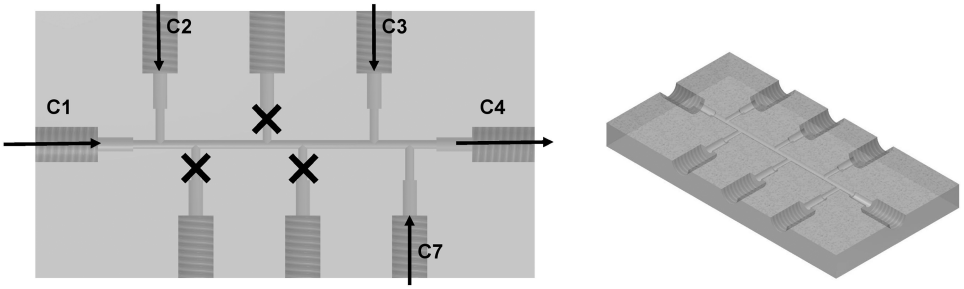

Figure 10. Segmented flow design of an eight-channel T-shaped FEP chip with C1, C2, and C3 as the inlet for the carrier medium TD (C1), iron salt (C2), and base (C3) and C4 as the outlet (left). Three-dimensional cut of the chip design (right).

Both platelet morphology, obtained by imaging techniques, and iron content determined by AAS allow understanding characteristics of particles produced under different conditions. These results underline the potential combination of imaging techniques with an analytical method such as AAS to characterize the newly developed nanoparticles.

Limitations and Future Perspective. Even though we have identified a protocol for the better synthesis of qualified SPION, further magnetic characterization with magnetic particle spectroscopy (MPS) and magnetic resonance imaging (MRI) of the obtained nanoparticles could be helpful to further understand the properties of the particles before *in vivo* studies. This analysis allows us to obtain the magnetization efficiency and the tomographic quality of the particles. Furthermore, it is possible to confirm the coating material bound to the particles using Fourier transform infrared (FT-IR) spectroscopy to further improve the quality of particles. We have previously proved that human serum albumin (HSA)-coated Ferucarbotran iron oxide particles (*i.e.*, the Resovit without polymer coating) improved platelet labeling.[33] It is, therefore, important to compare the capacity of our developed particles (the SP2) with the HSA-coated particles in labeling platelets. The equal or improved labeling ability indicates that our synthesis particles have a high potential for medical applications as HSA-coated particles can cause the release of proteins.

CONCLUSIONS

We have successfully optimized a protocol for the synthesis of biocompatible SPION *via* a coprecipitation method under continuous and segmented flows. Compared to the synthesis by batch, microfluidic synthesis reduces the reaction time and operating temperature and does not require an inert gas atmosphere. Depending on the synthesis methods and reaction conditions, the physicochemical and magnetic properties of the particles differ. The best conditions for the synthesis of the smallest particles with high stability were identified at an iron salt concentration ratio of 4.3/8.6, pH 10.8 (6.5 mM NH_4OH), and 20 mg/mL CMD coating. Continuous flow allowed for the production of particles of the smallest size down to approximately 100 nm, followed by segmented flow, while largest particles were obtained by batch synthesis. Particles were successfully coated with CMD or D70. The resulting CMD-coated particles showed higher stability of dispersion than D70-coated particles. The CMD-coated particles under a continuous flow exhibited superparamagnetic behavior, which is comparable with that of Resovist. Platelets uptake CMD-coated particles with higher efficiency than the Resovist, while D70-coated particles impaired platelets. We provide a helpful protocol for the synthesis of biocompatible SPION for not only platelet labeling but also other medical applications.

MATERIALS AND METHODS

Chemicals and Materials. Iron salts $FeCl_2{\cdot}4H_2O$, $FeCl_3{\cdot}6H_2O$, and $FeSO_4{\cdot}7H_2O$; ammonia water (25%); sodium hydroxide (NaOH); carboxymethyl dextran (CMD) of 10 kDa; dextran of 70 kDa (D70); tetradecane (TD) (Sigma-Aldrich, Holzkirchen, Germany); Resovist (provided by nanoPET Pharma GmbH, Berlin, Germany for research only); poly(tetrafluoroethylene) (PTFE) and fluorethylenpropylen (FEP) tubes (Jasco GmbH, Pfungstadt, Germany); ferrules and fittings (Besta Technik GmbH, Wilhelmsfeld, Germany); dialysis kit (spectra red, molecular weight cut-off (MWCO): 20 kDa) (Fisher Scientific GmbH, Osterode/Harz, Germany, and Carl Roth GmbH, Karlsruhe, Germany); and four-channel X-shaped micromixer and divider from polyether ether ketone (PEEK) (VDS Optilab GmbH, Berlin, Germany) were used. For the monitoring of the droplet generation, a reflex camera (Canon EOS 2000D) was used.

Ethics. The use of human blood obtained from healthy volunteers including the informed consent procedure was approved by the ethics board of Thuringia, Germany.

Synthesis of SPION. The synthesis strategy is based on the coprecipitation process from Massart.[70] For the microfluidic setup, an external actuator as a modular high-precision syringe pump Nemesys (Cetoni GmbH, Korbussen, Germany) was employed for accurate dosing and control of inlet flow rates for both continuous and segmented flow regimes. For the continuous flow, the inlet (C1−C3) and outlet channels (C4) of the commercial X-shaped micromixer have a diameter of 0.5 mm (Figure 12). For the segmented flow setup, all inlet/outlet capillaries (d_{in} = 1 mm) were custom made from Teflon-based polymer (FEP) to avert particle deposition and chip fouling. The eight-channel T-shaped design has several inlets and one outlet, while the screw thread was drilled from one FEP piece (Figure 10). The amount of different channels allows for varying the synthesis conditions and the dosing steps between the reactants.

The heating module to reach the reaction temperature consisted of a Peltier block in which the tube deposit was milled directly. To prevent sticking of the droplets inside the tubes during the tempering, the tube mounting within the thermoblock is cylindrical (Figure 11). The temperature of the reaction process can be varied between 30 and 100 °C with a temperature variation of 0.1 °C (manual instruction of the Peltier-based unit).

Continuous Flow. The setup consists of a commercial four-channel X-shaped micromixer with a polyether ether ketone (PEEK) material and an inner diameter of 0.5 mm, which was performed for the mixing of iron chloride solutions ($FeCl_2{\cdot}4H_2O/FeCl_3{\cdot}6H_2O$) with ammonia (12.9−3.9 M). To prevent clogging, water was dosed together with the reactant mixture within the mixer (Figure 12).

The flow rate during the synthesis process was 300 μL/min for every channel. First, the iron (II/III) chloride solution was mixed with the coating polymer (CMD or D70) outside the fluidic setup. Then, this solution was pumped *via* syringe 3 (S3) into the inlet of channel

https://doi.org/10.1021/acsami.2c13156
ACS Appl. Mater. Interfaces 2022, 14, 48011−48028

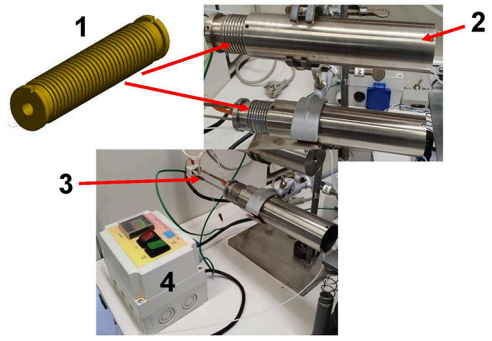

Figure 11. Heating module with the tube mounting for heat cartridge for 1.6 mm as diameter (1), the tube mounting cap (2), the thermocouple Pt-100 (3), and the thermostat with the power cable (4).

C2 and mixed with ammonia (NH_4OH), which was pumped *via* syringe 2 (S2) into the inlet of channel C1 and water from syringe 1 (S1) into the inlet of channel C3. After the mixing of the educts, the generated black solution was pumped from the outlet channel C4 and was heated in the special heating module at 60−70 °C where the tube was wound up directly on the fan convector for 30−60 min. After the synthesis, the product was sampled in a collector and dialyzed for 3 days to wash and purify the product from the impurities of the educts till the pH reached 7. The ready-to-use dialysis tubing (Spectra/Por Float-A-Lyzer, Thermo Fisher Scientific Inc., Germany) with a cellulose ester membrane of an MWCO of 20 kDa and a volume of 5 mL was used. Water (1 L) was used as the external solvent, while dialysis and the buffer exchange were carried out every 4 h, four times.

Segmented Flow. Contrary to the continuous flow, the small PEEK mixer setup was changed to a fluorethylenpropylen (FEP) polymer-based chip within eight channels (Figure 13). This design allows the addition of the reactants separately, and to form droplets and prevent them from being mixed, tetradecane (TD) was used as the carrier fluid. Also, a droplet distance control was integrated within the chip design which avoids droplet coalescence during the reaction process inside the heating unit. Before the droplet generation and the synthesis start, the iron precursor (iron(II) and (III) chloride mixture) was mixed with the coating agent as described in the continuous flow synthesis. The flow rates were adjusted that first the iron precursor (iron(II) and (III) chloride mixture) was pumped into the inlet of channel 2 (C2) and was injected into the carrier stream of TD, which was pumped into the inlet of channel 1 (C1) to produce a volume of nanoliter droplets (800 nL). Second, the base from the inlet channel 3 (C3) was dosed into the iron chloride droplets passively.

The distance between the generated droplets was spread by pumping of the carrier fluid TD into the inlet channel 7 (C7). For a uniform division of the carrier medium, a commercial divider from PEEK was integrated. The channels C3, C5, and C6 were closed. In the end and due to its density ($d_{TD} < d_{H_2O}$), TD was easily separated from the nanoparticles suspension once collected in the sample collector (Figure 13). The flow rate of each channel in continuous and segmented flow regimes was 300 μL/min. The reaction occurs immediately after the mixing of the reactants in the reaction chamber. The magnetite (Fe_3O_4) particles were formed, and the conversion to the product could be followed by a change in the solution color from light brown to black. Fe_3O_4 suspension was transported inside the PTFE tubes to the same stainless steel heaters that were used for the synthesis with the continuous flow to heat up to 60 and 70 °C, taking a reaction time of approximately 30−60 min and collected for subsequent analysis.

Synthesis by Batch. In a 100 mL flask, a mixture of $FeCl_2{\cdot}7H_2O$ and $FeCl_3{\cdot}6H_2O$ at a ratio of 1:2 was dissolved into 25 mL of deionized water, and 25 mL of a solution containing a dextran-based coating agent (CMD or D70) was added and stirred together under cooled conditions (4 °C). Another 25 mL basic solution of ammonium hydroxide (NH_4OH) was prepared in a different flask. Then, ammonium hydroxide was added dropwise (1 mL/min) to the cold iron salt and coating agent solution till the pH reached 10.8. The solution was heated to 90 °C for 1 h under an argon atmosphere and intensive stirring (500 rpm). Subsequently, the black solution was dialyzed for 3 days to wash and purify the product from the impurities of the educts till the pH was 7. Sample dialysis was performed as described in the last section.

Characterization of Synthesized Magnetic Nanoparticles. *X-ray Diffraction (XRD).* For the crystal structure, average particle size and the concentration of impurity compounds present were characterized. A MAC Science MXP18 X-ray diffractometer was used for X-ray diffraction patterns of these samples. The 2θ values were taken from 20 to 110° with a step size of 0.04° using Cr Kα radiation (λ value of 2.2897 Å). The freeze-dried samples were dusted onto plates with low background. A small quantity of 30 ± 2 mg spread over a 5 cm^2 area was used to minimize the error in the peak location, and also the broadening of peaks due to the thickness of the sample was reduced. This data illustrates the crystal structure of the particles and also provides the interplanar space. The XRD patterns of the nanoparticles were verified by comparison with the ICDD database. The broadening of the peak was related to the average

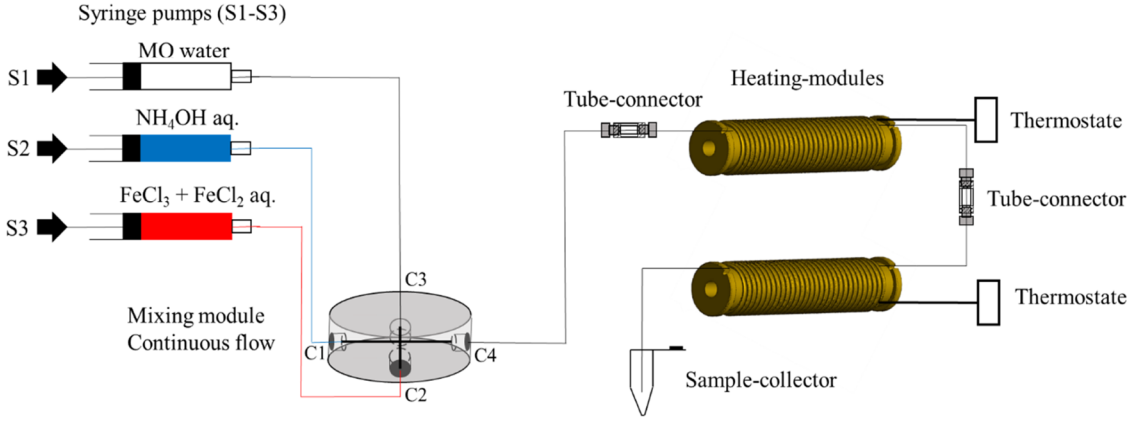

Figure 12. Schematic setup of the continuous flow. Flow regime for SPION synthesis with a three-channel syringe pump and with a four-channel X-shaped PEEK mixer. To prevent agglomeration clogging, water was added to the reactants from inlet channel C3 *via* syringe 1 (S1), while the base (NH_4OH) and the iron precursor ($FeCl_3$ and $FeCl_2$) with the polymer coating agents (CMD or D70) were pumped with syringes 2 (S2) and 3 (S3) into the inlet of the channels C1 and C2. The flow rate for every used channel was 300 μL/min. To guarantee an undisturbed transport of the reactants inside the tubes, microfluidic tube connectors were used.

https://doi.org/10.1021/acsami.2c13156
ACS Appl. Mater. Interfaces 2022, 14, 48011−48028

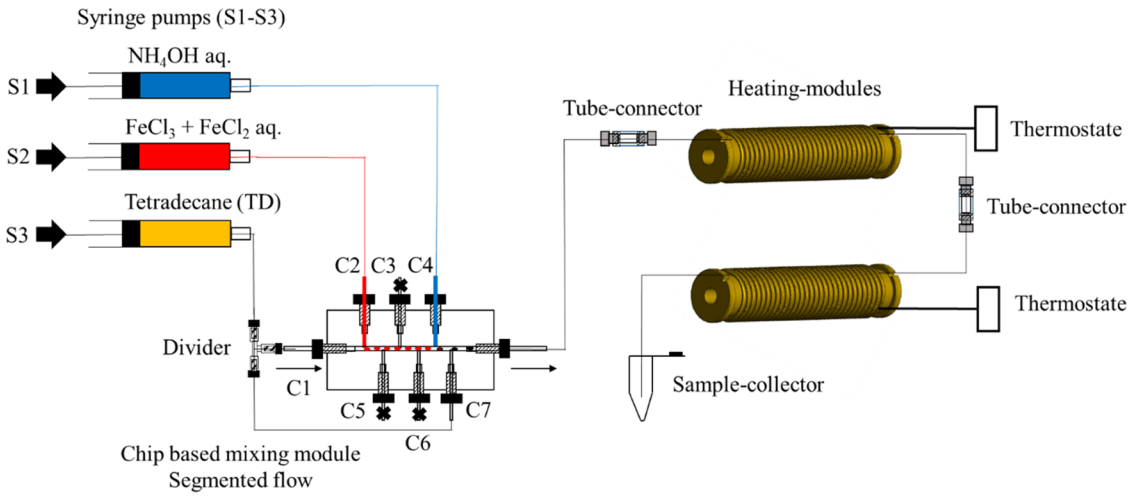

Figure 13. Setup of the segmented flow regime for SPION synthesis with a three-channel syringe pump and eight-channel FEP chip and tetradecane (TD) as a carrier fluid. Then, channels 3, 5, and 6 (C3, C5, C6) were closed (black cross) and filled with TD to avoid air bubbles during the synthesis process. To prevent a droplet break between the different modules during the transport, tube connectors were used. A droplet coalescence was avoided with an integrated tool that uniformly divided the carrier medium TD stream. The process of SPION production began with the droplet generation of the iron chloride mixture (red) pumped with syringe 2 (S2) from the inlet channel 2 (C2) into the main channel. The carrier fluid (orange colored), which was pumped from the inlet channel 1 (C1) into the main channel as well, sheared the aqueous iron chloride solution into droplets of 800 nL. The reaction began immediately after passive dosing of base (NH_4OH; blue) to the iron chloride droplets. The base was pumped with syringe 1 (S1) into the inlet channel 4 (C4). Additionally, the droplet spreading to prevent droplet coalescence was done by pumping of carrier medium into the inlet channel 7 (C7).

diameter (L) of the particle according to Scherrer's formula, *i.e.*, $L = 0.9\lambda/\Delta \cos\theta$, where λ is X-ray wavelength, Δ is line broadening measured at half-height, and θ is Bragg angle of the particles. The average particle size is obtained from the most intense peak, corresponding to (311) reflection in magnetite using the Debye–Scherrer formula.

Thermogravimetric Analysis (TGA). Thermogravimetric analysis of the dried samples was performed using a Mettler-Toledo TGA 850 under a nitrogen atmosphere at a heating rate of 12.5 K/min from 25 to 800 °C to monitor the mass loss of 10 mg of polymer-coated SPIONs.

Superconducting Quantum Interference Device (SQUID) Magnetometer. For static M/H magnetization measurements, an MPMSXL 5 (QuantumDesign) was used. Magnetization values were normalized to the volume fraction of magnetite. These measurements were taken from 0.125 Oe to ±125 kOe field (1 Oe = 79.577 A/m). From these field *versus* magnetization curve patterns, saturation magnetization values of the samples were determined.

Transmission Electron Microscopy (TEM). The size and shape of SPION were detected with FEI Tecnai G^2 20 S-TWIN (FEI Company, OR) with a LAB_6 cathode, an acceleration voltage of 200 kV, and a dot resolution of 0.24 nm. One drop of magnetite dispersion was placed on a carbon-coated copper grid (0.3 cm in diameter, mesh size of 200 holes/cm) and left to dry overnight at room temperature (RT) (25 °C).

Dynamic Light Scattering (DLS). The sizes and surface ζ potential of SPION were determined by dynamic light scattering (DLS, Zetasizer Nano ZS, Malvern Instruments Ltd., Worcestershire, U.K.). DLS measurement was continuously carried out at 25 °C for 30 min in water using disposal cuvettes (Sigma-Aldrich, St. Louis). The measured average hydrodynamic sizes and SD were analyzed. Additionally, DLS was used to determine the ζ potential of the different SPION. They were diluted in a concentration range of 0.0125–0.1 mM with water and measured in a folded capillary at 25 °C with six repetitions. Data analysis was performed with Origin software (version 7.5). The one-way analysis of variance (ANOVA) was used to determine any significant differences in sizes among particles. To determine the stability of particles, the hydrodynamic diameter was measured within 19 months. Samples including CMD-coated particles under batch, continuous, and segmented flows were stored at 6 °C before measurements.

Isolation of Human Platelets. Human blood from healthy donors who were drug-free within the previous 10 days was collected into a tube of ACD-A 1.5 mL BD-Vacutainer (Germany). The blood tube was sealed with parafilm and rested at room temperature for 15 min. Platelet-rich plasma (PRP) was first obtained by centrifugation at 120*g* for 20 min at room temperature. To isolate platelets, PRP in the presence of 15% acid citrate dextrose (ACD-A, Fresenius Kabi, Germany) and 2.5 U/mL apyrase (grade IV SIGMA, Munich, Germany) were centrifuged at 650*g* for 7 min. The platelet pellet was resuspended in buffer pH 6.3 composed of 137 mM NaCl, 2.7 mM KCl, 11.9 mM $NaHCO_3$, 0.4 mM Na_2HPO_4, and 2.5 U/mL hirudin and incubated for 15 min at 37 °C before centrifuging at 650*g* for 7 min. Platelet pellets were again carefully resuspended in suspension buffer and adjusted to a concentration of 300×10^9/L using a blood counter (pocH-100i, SYMEX, Germany) and then incubated for 45 min at 37 °C before use.

Platelet Labeling with Synthesized SPION. Isolated platelets of 100 μL (300 000 platelets/μL) were gently mixed with 100 μL SPION suspensions (2 mM final) and incubated at 37 °C for 30 min. After that, the suspensions were washed two times with an apyrase-based washing buffer to eliminate the excess iron particles by centrifugation at 650*g* for 7 min. After discarding the remaining solution, platelet pellets were resuspended in 100 μL washing buffer.

Confocal Laser Scanning Microscopy (CLMS). A confocal microscope (LSM 710 examiner z1) was used to track the changes in the shape of platelets after they uptake SPION. The SPION-labeled platelets were then fixed with PFA (4%) final for 30 min at RT. Then, the samples were washed two times with the washed buffer to remove the excess PFA. To stain platelets, the samples were incubated overnight at 4 °C with Alexa Fluor 647 antihuman CD42a antibody (Biolegend, San Diego) with a concentration of 1:1000 in phosphate-buffered saline (PBS). Finally, the samples were washed with PBS, covered with a thin glass slide, and imaged with Zeiss LSM 710 (Carl Zeiss, Gottingen, Germany) at room temperature (RT) in the dark. The filter of 638–755, a pixel dwell of 12.6 μs, a laser power of 633 nm (2.0%), and a master gain of 1050 were used. We have now integrated this into the CLSM method. The areas of single platelets were quantified by ImageJ software.

https://doi.org/10.1021/acsami.2c13156
ACS Appl. Mater. Interfaces 2022, 14, 48011–48028

Quantitative Cellular Iron Determination by Atomic Absorption Spectroscopy (AAS). For cell labeling, isolated platelets of 100 μL (30 000 platelets/μL) were gently mixed with 100 μL SPION suspensions (4 mM) and incubated at 37 °C for 30 min. After that, the suspensions were washed two times at 650*g* for 7 min with an apyrase-based washing buffer to eliminate the excess iron particles. After discarding the remaining solution, platelet pellets were resuspended in 100 μL washing buffer. The cellular iron content was determined utilizing atomic absorption spectroscopy (AAS). SPION suspensions of different concentrations, including 0 mg (control) and 3.58 mg, were incubated with washed platelets in SSP+ buffer using the appropriate protocol. Second, the samples were centrifuged at 1400*g* for 5 min to discard the supernatants. Subsequently, 500 μL of trypsin (0.5%) in PBS and 500 μL of SDS solution (0.2%) in water were added to platelet pellets and incubated at 37 °C for 30 min. The samples were then pooled with their respective supernatants and transferred to the decontaminated 10 mL flasks containing 1 mL of HNO_3 (12 N) and 500 μL of H_2O_2 (30%) (Sigma-Aldrich) and heated until reaching a boiling point. Finally, the samples were cooled down and diluted to 5 mL with water before AAS measurements. Iron content per platelet was measured in triplicate using an iron calibration graph with a commercial iron standard ranging from 0 to 150 μg/L by a contrAA 700 atomic absorption spectrometer (Analytik Jena, Jena, Germany).

White Light Interferometry (WLI). WLI was used to identify the height changes of platelets after labeling with SPION. The same protocol for sample preparation for SEM experiments was applied for WLI. The surface roughness of the samples was measured using a Bruker contour GTK-3D optical microscope (Bruker Nano GmbH, Berlin, Germany), vertical scanning option of 5× magnification. A measurement area of X = 1266.2 μm, Y = 949.6 μm, and a lateral sampling of 1.978 μm with a resolution of 640 × 480 pixel^2 were observed. The images were further analyzed with SPIP (version, 6.6.5, Image Metrology, Kongens Lyngby, Denmark). A manual level tilt compensation and a filter wavelength of ISO 16610 Gaussian L filter 1/7 of the lateral measurement dimensions were applied according to ISO 25178-2 to remove form and waviness and to calculate the arithmetical mean height (Sa). The roughness obtained was taken from five points on the sample surface, while the average and standard deviation were calculated using Microsoft Excel (version 16).

Scanning Electron Microscopy (SEM). Platelet morphology and cell aggregation were screened by SEM (Carl Zeiss AG, Jena, Germany). Images were taken with a magnification of 200× and 500×. Round glass coverslips (Plano GmbH, Wetzlar, Germany) of 24 mm were autoclaved and sonicated with 80% ethanol. The labeled platelets were incubated on glass coverslips for 15 min at RT. Then, the samples were washed with PBS and covered with 4% paraformaldehyde for 3 h at RT. Subsequently, the samples were washed twice with PBS, followed by an ascending isopropanol series (30, 50, 70, 90, and 100%) for dewatering. Each incubation was carried out for 10 min at RT. The samples were then incubated with 50% hexamethyldisilazane (HMDS) + 50% isopropanol for 10 min at RT. The samples were then covered with 100% HMDS and allowed to dry overnight. Finally, a thin Au layer was sputtered on the sample surface.

■ ASSOCIATED CONTENT

Supporting Information

The Supporting Information is available free of charge at https://pubs.acs.org/doi/10.1021/acsami.2c13156.

SPION coated with different concentrations of CMD or D70 and tendency for stable SPION solution (Figure S1); stabilization of CMD-coated SPION determined by DLS and variation at different batch and fluidic regimes (Figure S2); SEM images for the platelets labeled with SPION and agglomeration tendency depending on parameters and media (Figure S3); determination of height changes of platelets labeled with SPION by WLI and monitoring morphology of platelets with SPION (Figure S4) (PDF)

■ AUTHOR INFORMATION

Corresponding Authors

Jörg Schemberg − *Institute for Bioprocessing and Analytical Measurement Techniques (iba), 37308 Heiligenstadt, Germany*; Email: joerg.schemberg@iba-heiligenstadt.de

Thi-Huong Nguyen − *Institute for Bioprocessing and Analytical Measurement Techniques (iba), 37308 Heiligenstadt, Germany; Institute for Chemistry and Biotechnology, Faculty of Mathematics and Natural Sciences, Technische Universität Ilmenau, 98694 Ilmenau, Germany;* orcid.org/0000-0002-9237-3482; Email: thi-huong.nguyen@iba-heiligenstadt.de

Authors

Abdelouahad El Abbassi − *Institute for Bioprocessing and Analytical Measurement Techniques (iba), 37308 Heiligenstadt, Germany*

Annerose Lindenbauer − *Institute for Bioprocessing and Analytical Measurement Techniques (iba), 37308 Heiligenstadt, Germany*

Li-Yu Chen − *Institute for Bioprocessing and Analytical Measurement Techniques (iba), 37308 Heiligenstadt, Germany; Department of Infection Biology, Leibniz Institute for Natural Product Research and Infection Biology, 07745 Jena, Germany*

Andreas Grodrian − *Institute for Bioprocessing and Analytical Measurement Techniques (iba), 37308 Heiligenstadt, Germany*

Xenia Nakos − *Institute for Bioprocessing and Analytical Measurement Techniques (iba), 37308 Heiligenstadt, Germany*

Gurunath Apte − *Institute for Bioprocessing and Analytical Measurement Techniques (iba), 37308 Heiligenstadt, Germany; Institute of Nanotechnology (INT) and Karlsruhe Nano Micro Facility, Karlsruhe Institute of Technology, 76131 Karlsruhe, Germany;* orcid.org/0000-0002-4391-2152

Nida Khan − *Institute for Bioprocessing and Analytical Measurement Techniques (iba), 37308 Heiligenstadt, Germany; Institute for Chemistry and Biotechnology, Faculty of Mathematics and Natural Sciences, Technische Universität Ilmenau, 98694 Ilmenau, Germany*

Alexander Kraupner − *nanoPET GmbH, 10115 Berlin, Germany*

Gunter Gastrock − *Institute for Bioprocessing and Analytical Measurement Techniques (iba), 37308 Heiligenstadt, Germany*

Complete contact information is available at: https://pubs.acs.org/10.1021/acsami.2c13156

Author Contributions

J.S. and A.E.A. synthesized SPION, performed AAS experiments, and analyzed data. A.G. constructed the chips for the segmented flow and the tube-based temperature unit. A.K. performed TEM, TGA, and SQUID magnetometry. A.L. performed DLS experiments, and T.-H.N. analyzed DLS results. L.-Y.C. performed and analyzed CLMS experiments, N.K. performed WLI imaging, and G.A. performed SEM experiments. X.N. supported with AAS experiments. G.G.

https://doi.org/10.1021/acsami.2c13156
ACS Appl. Mater. Interfaces 2022, 14, 48011−48028

supported with some theoretical interpretations of the magnetic particle properties and the microfluidic setups and conceived the project SyNMAG together with J.S. J.S. and T.-H.N. conceived the project, designed experiments, interpreted the data, and wrote the manuscript. All authors read and agreed to the final version of the manuscript.

Funding

This work was supported by the German Federal Ministry of Education and Research (SyNMAG; grant no. 13XP5095A), the Free State of Thuringia, Germany, and partially supported by the Deutsche Forschungsgemeinschaft (DFG, Project numbers: 269095734 and 469240103).

Notes

The authors declare no competing financial interest.

■ ACKNOWLEDGMENTS

We thank the Dialysis Eichsfeld for helping with the platelet donation, members of the faculty of inorganic and analytical chemistry at the Johannes Gutenberg University in Mainz for the TEM measurements of SPION, Holger Rothe for supporting with white light interferometry measurements and analysis, and Dr. Karen Lemke for revising our manuscript.

■ REFERENCES

(1) Teston, E.; Maldiney, T.; Marangon, I.; Volatron, J.; Lalatonne, Y.; Motte, L.; Boisson-Vidal, C.; Autret, G.; Clément, O.; Scherman, D.; et al. Nanohybrids with Magnetic and Persistent Luminescence Properties for Cell Labeling, Tracking, In Vivo Real-Time Imaging, and Magnetic Vectorization. *Small* **2018**, *14*, No. 1800020.

(2) Li, X.; Wei, J.; Aifantis, K. E.; Fan, Y.; Feng, Q.; Cui, F. Z.; Watari, F. Current investigations into magnetic nanoparticles for biomedical applications. *J. Biomed. Mater. Res., Part A* **2016**, *104*, 1285−1296.

(3) Castaneda, R. T.; Khurana, A.; Khan, R.; Daldrup-Link, H. E. Labeling stem cells with ferumoxytol, an FDA-approved iron oxide nanoparticle. *J. Visualized Exp.* **2011**, *57*, No. e3482.

(4) Bartolozzi, C.; Lencioni, R.; Donati, F.; Cioni, D. Abdominal MR: liver and pancreas. *Eur. Radiol.* **1999**, *9*, 1496−1512.

(5) Panagiotopoulos, N.; Duschka, R. L.; Ahlborg, M.; Bringout, G.; Debbeler, C.; Graeser, M.; Kaethner, C.; Lüdtke-Buzug, K.; Medimagh, H.; Stelzner, J.; et al. Magnetic particle imaging: current developments and future directions. *Int. J. Nanomed.* **2015**, *10*, 3097.

(6) Colombo, M.; Carregal-Romero, S.; Casula, M. F.; Gutiérrez, L.; Morales, M. P.; Böhm, I. B.; Heverhagen, J. T.; Prosperi, D.; Parak, W. J. Biological applications of magnetic nanoparticles. *Chem. Soc. Rev.* **2012**, *41*, 4306−4334.

(7) Périgo, E. A.; Hemery, G.; Sandre, O.; Ortega, D.; Garaio, E.; Plazaola, F.; Teran, F. J. Fundamentals and advances in magnetic hyperthermia. *Appl. Phys. Rev.* **2015**, *2*, No. 041302.

(8) Efremova, M. V.; Naumenko, V. A.; Spasova, M.; Garanina, A. S.; Abakumov, M. A.; Blokhina, A. D.; Melnikov, P. A.; Prelovskaya, A. O.; Heidelmann, M.; Li, Z.-A.; et al. Magnetite-Gold nanohybrids as ideal all-in-one platforms for theranostics. *Sci. Rep.* **2018**, *8*, No. 11295.

(9) Hayashi, K.; Nakamura, M.; Miki, H.; Ozaki, S.; Abe, M.; Matsumoto, T.; Sakamoto, W.; Yogo, T.; Ishimura, K. Magnetically responsive smart nanoparticles for cancer treatment with a combination of magnetic hyperthermia and remote-control drug release. *Theranostics* **2014**, *4*, 834.

(10) Lin, L. S.; Yang, X.; Zhou, Z.; Yang, Z.; Jacobson, O.; Liu, Y.; Yang, A.; Niu, G.; Song, J.; Yang, H. H.; Chen, X. Yolk−shell nanostructure: an ideal architecture to achieve harmonious integration of magnetic−plasmonic hybrid theranostic platform. *Adv. Mater.* **2017**, *29*, No. 1606681.

(11) Apte, G.; Lindenbauer, A.; Schemberg, J.; Rothe, H.; Nguyen, T.-H. Controlling Surface-Induced Platelet Activation by Agarose and Gelatin-Based Hydrogel Films. *ACS Omega* **2021**, *6*, 10963−10974.

(12) Karimzadeh, I.; Aghazadeh, M.; Ganjali, M. R.; Norouzi, P.; Shirvani-Arani, S.; Doroudi, T.; Kolivand, P. H.; Marashi, S. A.; Gharailou, D. A novel method for preparation of bare and poly (vinylpyrrolidone) coated superparamagnetic iron oxide nanoparticles for biomedical applications. *Mater. Lett.* **2016**, *179*, 5−8.

(13) Gnanaprakash, G.; Philip, J.; Jayakumar, T.; Raj, B. Effect of digestion time and alkali addition rate on physical properties of magnetite nanoparticles. *J. Phys. Chem. B* **2007**, *111*, 7978−7986.

(14) Wang, J.; Deng, T.; Dai, Y. Study on the processes and mechanism of the formation of Fe3O4 at low temperature. *J. Alloys Compd.* **2005**, *390*, 127−132.

(15) Mascolo, M. C.; Pei, Y.; Ring, T. A. Room temperature co-precipitation synthesis of magnetite nanoparticles in a large pH window with different bases. *Materials* **2013**, *6*, 5549−5567.

(16) Jahn, A.; Reiner, J. E.; Vreeland, W. N.; DeVoe, D. L.; Locascio, L. E.; Gaitan, M. Preparation of nanoparticles by continuous-flow microfluidics. *J. Nanopart. Res.* **2008**, *10*, 925−934.

(17) Chen, D.; Love, K. T.; Chen, Y.; Eltoukhy, A. A.; Kastrup, C.; Sahay, G.; Jeon, A.; Dong, Y.; Whitehead, K. A.; Anderson, D. G. Rapid discovery of potent siRNA-containing lipid nanoparticles enabled by controlled microfluidic formulation. *J. Am. Chem. Soc.* **2012**, *134*, 6948−6951.

(18) Zhu, P.; Wang, L. Passive and active droplet generation with microfluidics: a review. *Lab Chip* **2017**, *17*, 34−75.

(19) Lu, Y.; Fu, T.; Zhu, C.; Ma, Y.; Li, H. Z. Pinch-off mechanism for Taylor bubble formation in a microfluidic flow-focusing device. *Microfluid. Nanofluid.* **2014**, *16*, 1047−1055.

(20) Chung, A. J. A minireview on inertial microfluidics fundamentals: Inertial particle focusing and secondary flow. *BioChip J.* **2019**, *13*, 53−63.

(21) Nightingale, A. M.; deMello, J. C. Segmented flow reactors for nanocrystal synthesis. *Adv. Mater.* **2013**, *25*, 1813−1821.

(22) Gonidec, M.; Puigmartí-Luis, J. Continuous-versus segmented-flow microfluidic synthesis in materials science. *Crystals* **2019**, *9*, No. 12.

(23) Lin, S.; Lin, K.; Lu, D.; Liu, Z. Preparation of uniform magnetic iron oxide nanoparticles by co-precipitation in a helical module microchannel reactor. *J. Environ. Chem. Eng.* **2017**, *5*, 303−309.

(24) Karim, A. M.; Al Hasan, N.; Ivanov, S.; Siefert, S.; Kelly, R. T.; Hallfors, N. G.; Benavidez, A.; Kovarik, L.; Jenkins, A.; Winans, R. E.; Datye, A. K. Synthesis of 1 nm Pd nanoparticles in a microfluidic reactor: insights from in situ X-ray absorption fine structure spectroscopy and small-angle X-ray scattering. *J. Phys. Chem. C* **2015**, *119*, 13257−13267.

(25) James, M.; Revia, R. A.; Stephen, Z.; Zhang, M. Microfluidic Synthesis of Iron Oxide Nanoparticles. *Nanomaterials* **2020**, *10*, No. 2113.

(26) Michelson, A. D.*Platelets*, 3rd ed.; Academic Press/Elsevier, 2013.

(27) Nguyen, T.-H.; Palankar, R.; Bui, V.-C.; Medvedev, N.; Greinacher, A.; Delcea, M. Rupture forces among human blood platelets at different degrees of activation. *Sci. Rep.* **2016**, *6*, No. 25402.

(28) Michelson, A. D.*Platelets*; Elsevier Science, 2013.

(29) Smyth, S. S.; Parise, L. V. Regulation of ligand binding to glycoprotein IIb-IIIa (integrin αIIb β 3) in isolated platelet membranes. *Biochem. J.* **1993**, *292*, 749−758.

(30) Whiteheart, S. W. Platelet granules: surprise packages. *Blood* **2011**, *118*, 1190−1191.

(31) Decristoforo, C.; Penuelas, I.; Patt, M.; Todde, S. European regulations for the introduction of novel radiopharmaceuticals in the clinical setting. *Q. J. Nucl. Med. Mol. Imaging* **2017**, *61*, 135.

(32) Aurich, K.; Spoerl, M. C.; Furll, B.; Sietmann, R.; Greinacher, A.; Hosten, N.; Weitschies, W. Development of a method for magnetic labeling of platelets. *Nanomedicine* **2012**, *8*, 537−544.

https://doi.org/10.1021/acsami.2c13156
ACS Appl. Mater. Interfaces 2022, 14, 48011−48028

(33) Nguyen, T. H.; Schuster, N.; Greinacher, A.; Aurich, K. Uptake Pathways of Protein-Coated Magnetic Nanoparticles in Platelets. *ACS Appl. Mater. Interfaces* **2018**, *10*, 28314−28321.
(34) Azcona, P.; Zysler, R.; Lassalle, V. Simple and novel strategies to achieve shape and size control of magnetite nanoparticles intended for biomedical applications. *Colloids Surf., A* **2016**, *504*, 320−330.
(35) Yoffe, S.; Leshuk, T.; Everett, P.; Gu, F. Superparamagnetic iron oxide nanoparticles (SPIONs): synthesis and surface modification techniques for use with MRI and other biomedical applications. *Curr. Pharm. Des.* **2013**, *19*, 493−509.
(36) Hauser, A. K.; Mathias, R.; Anderson, K. W.; Hilt, J. Z. The effects of synthesis method on the physical and chemical properties of dextran coated iron oxide nanoparticles. *Mater. Chem. Phys.* **2015**, *160*, 177−186.
(37) Sheng-Nan, S.; C, W.; Zan-Zan, Z.; Yang-Long, H.; Venkatraman, S. S.; Zhi-Chuan, X. Magnetic iron oxide nanoparticles: Synthesis and surface coating technoques for biomedical applications. *Chin. Phys. B* **2014**, *23*, No. 037503.
(38) Kamalzare, S.; Noormohammadi, Z.; Rahimi, P.; Atyabi, F.; Irani, S.; Tekie, F. S. M.; Mottaghitalab, F. Carboxymethyl dextran-trimethyl chitosan coated superparamagnetic iron oxide nanoparticles: An effective siRNA delivery system for HIV-1 Nef. *J. Cell. Physiol.* **2019**, *234*, 20554−20565.
(39) Javid, A.; Ahmadian, S.; Saboury, A. A.; Kalantar, S. M.; Rezaei-Zarchi, S. Chitosan-coated superparamagnetic iron oxide nanoparticles for doxorubicin delivery: synthesis and anticancer effect against human ovarian cancer cells. *Chem. Biol. Drug Des.* **2013**, *82*, 296−306.
(40) Khalkhali, M.; Rostamizadeh, K.; Sadighian, S.; Khoeini, F.; Naghibi, M.; Hamidi, M. The impact of polymer coatings on magnetite nanoparticles performance as MRI contrast agents: a comparative study. *Daru, J. Pharm. Sci.* **2015**, *23*, No. 45.
(41) Liu, Y.; Li, J.; Xu, K.; Gu, J.; Huang, L.; Zhang, L.; Liu, N.; Kong, J.; Xing, M.; Zhang, L.; Zhang, L. Characterization of superparamagnetic iron oxide nanoparticle-induced apoptosis in PC12 cells and mouse hippocampus and striatum. *Toxicol. Lett.* **2018**, *292*, 151−161.
(42) Homogen, M. Synthesis and physicochemical properties of magnetite nanoparticles (Fe3O4) as potential solid support for homogeneous catalysts. *Malays. J. Anal. Sci* **2018**, *22*, 768−774.
(43) Yoshida, T.; Enpuku, K.; Ludwig, F.; Dieckhoff, J.; Wawrzik, T.; Lak, A.; Schilling, M.Characterization of Resovist Nanoparticles For Magnetic Particle Imaging. *Magnetic Particle Imaging*; Springer, 2012; pp 3−7.
(44) Vasić, K.; Knez, Ž.; Konstantinova, E. A.; Kokorin, A. I.; Gyergyek, S.; Leitgeb, M. Structural and magnetic characteristics of carboxymethyl dextran coated magnetic nanoparticles: From characterization to immobilization application. *React. Funct. Polym.* **2020**, *148*, No. 104481.
(45) Petcharoen, K.; Sirivat, A. Synthesis and characterization of magnetite nanoparticles via the chemical co-precipitation method. *Mater. Sci. Eng., B* **2012**, *177*, 421−427.
(46) Aurich, K.; Wesche, J.; Palankar, R.; Schluter, R.; Bakchoul, T.; Greinacher, A. Magnetic Nanoparticle Labeling of Human Platelets from Platelet Concentrates for Recovery and Survival Studies. *ACS Appl. Mater. Interfaces* **2017**, *9*, 34666−34673.
(47) Ali, A.; Zafar, H.; Zia, M.; Haq, I.; Phull, A.; Ali, J.; Hussain, A. Synthesis, characterization, applications, and challenges of iron oxide nanoparticles. *Nanotechnol., Sci. Appl.* **2016**, *9*, 49−67.
(48) Maity, D.; Agrawal, D. Synthesis of iron oxide nanoparticles under oxidizing environment and their stabilization in aqueous and non-aqueous media. *J. Magn. Magn. Mater.* **2007**, *308*, 46−55.
(49) LaMer, V. K.; Dinegar, R. H. Theory, production and mechanism of formation of monodispersed hydrosols. *J. Am. Chem. Soc.* **1950**, *72*, 4847−4854.
(50) Christian, P.; Von der Kammer, F.; Baalousha, M.; Hofmann, T. Nanoparticles: structure, properties, preparation and behaviour in environmental media. *Ecotoxicology* **2008**, *17*, 326−343.
(51) Shevchenko, E. V.; Talapin, D. V.; Schnablegger, H.; Kornowski, A.; Festin, Ö.; Svedlindh, P.; Haase, M.; Weller, H. Study of nucleation and growth in the organometallic synthesis of magnetic alloy nanocrystals: the role of nucleation rate in size control of CoPt3 nanocrystals. *J. Am. Chem. Soc.* **2003**, *125*, 9090−9101.
(52) Lohse, S. E.; Eller, J. R.; Sivapalan, S. T.; Plews, M. R.; Murphy, C. J. A simple millifluidic benchtop reactor system for the high-throughput synthesis and functionalization of gold nanoparticles with different sizes and shapes. *ACS Nano* **2013**, *7*, 4135−4150.
(53) Jun, H.; Fabienne, T.; Florent, M.; Coulon, P. E.; Nicolas, M.; Olivier, S. Understanding of the size control of biocompatible gold nanoparticles in millifluidic channels. *Langmuir* **2012**, *28*, 15966−15974.
(54) Fu, F.; Li, P.; Wang, K.; Wu, R. Numerical Simulation of Sessile Droplet Spreading and Penetration on Porous Substrates. *Langmuir* **2019**, *35*, 2917−2924.
(55) Hassan, N.; Cabuil, V.; Abou-Hassan, A. Assembling magneto-plasmonic microcapsules using a microfluidic device. *Chem. Commun.* **2013**, *49*, 412−414.
(56) Seth, A.; Bealle, G.; Santanach-Carreras, E.; Abou-Hassan, A.; Menager, C. Design of vesicles using capillary microfluidic devices: from magnetic to multifunctional vesicles. *Adv. Mater.* **2012**, *24*, 3544−3548.
(57) Goya, G. F.; Berquo, T.; Fonseca, F.; Morales, M. Static and dynamic magnetic properties of spherical magnetite nanoparticles. *J. Appl. Phys.* **2003**, *94*, 3520−3528.
(58) Gutiérrez, L.; De la Cueva, L.; Moros, M.; Mazarío, E.; De Bernardo, S.; De la Fuente, J. M.; Morales, M. P.; Salas, G. Aggregation effects on the magnetic properties of iron oxide colloids. *Nanotechnology* **2019**, *30*, No. 112001.
(59) Huynh, K. A.; Chen, K. L. Aggregation kinetics of citrate and polyvinylpyrrolidone coated silver nanoparticles in monovalent and divalent electrolyte solutions. *Environ. Sci. Technol.* **2011**, *45*, 5564−5571.
(60) Mørup, S.; Hansen, M. F.; Frandsen, C. Magnetic interactions between nanoparticles. *Beilstein J. Nanotechnol.* **2010**, *1*, 182−190.
(61) Lalatonne, Y.; Richardi, J.; Pileni, M. Van der Waals versus dipolar forces controlling mesoscopic organizations of magnetic nanocrystals. *Nat. Mater.* **2004**, *3*, 121−125.
(62) Serantes, D.; Baldomir, D.; Martinez-Boubeta, C.; Simeonidis, K.; Angelakeris, M.; Natividad, E.; Castro, M.; Mediano, A.; Chen, D.-X.; Sanchez, A.; et al. Influence of dipolar interactions on hyperthermia properties of ferromagnetic particles. *J. Appl. Phys.* **2010**, *108*, No. 073918.
(63) Nadeem, K.; Krenn, H.; Traußnig, T.; Würschum, R.; Szabó, D.; Letofsky-Papst, I. Effect of dipolar and exchange interactions on magnetic blocking of maghemite nanoparticles. *J. Magn. Magn. Mater.* **2011**, *323*, 1998−2004.
(64) Jonsson, T.; Nordblad, P.; Svedlindh, P. Dynamic study of dipole-dipole interaction effects in a magnetic nanoparticle system. *Phys. Rev. B: Condens. Matter Mater. Phys.* **1998**, *57*, 497.
(65) Gavilán, H.; Sánchez, E. H.; Brollo, M. E.; Asín, L.; Moerner, K. K.; Frandsen, C.; Lázaro, F. J.; Serna, C. J.; Veintemillas-Verdaguer, S.; Morales, M. P.; Gutiérrez, L. Formation mechanism of maghemite nanoflowers synthesized by a polyol-mediated process. *ACS Omega* **2017**, *2*, 7172−7184.
(66) Maurizi, L.; Papa, A.-L.; Dumont, L.; Bouyer, F.; Walker, P.; Vandroux, D.; Millot, N. Influence of surface charge and polymer coating on internalization and biodistribution of polyethylene glycol-modified iron oxide nanoparticles. *J. Biomed. Nanotechnol.* **2015**, *11*, 126−136.
(67) Linh, P.; Phuc, N.; Hong, L.; Uyen, L.; Chien, N.; Nam, P.; Quy, N.; Nhung, H.; Phong, P.; Lee, I.-J. Dextran coated magnetite high susceptibility nanoparticles for hyperthermia applications. *J. Magn. Magn. Mater.* **2018**, *460*, 128−136.
(68) Apte, G.; Börke, J.; Rothe, H.; Liefeith, K.; Nguyen, T.-H. Modulation of Platelet-Surface Activation: Current State and Future Perspectives. *ACS Appl. Bio Mater.* **2020**, *3*, 5574−5589.

(69) Bui, V.-C.; Medvedev, N.; Apte, G.; Chen, L.-Y.; Denker, C.; Greinacher, A.; Nguyen, T.-H. Response of Human Blood Platelets on Nanoscale Groove Patterns: Implications for Platelet Storage. *ACS Appl. Nano Mater.* **2020**, *3*, 6996−7004.
(70) Massart, R. Preparation of aqueous magnetic liquids in alkaline and acidic media. *IEEE Trans. Magn.* **1981**, *17*, 1247−1248.

https://doi.org/10.1021/acsami.2c13156
ACS Appl. Mater. Interfaces 2022, 14, 48011−48028